Imperial College London

MSc Dissertation

Imperial College London

Department of Physics

Cosmology of the Stochastic Axion

Author:
Liina Jukko

Supervisor:
Prof. Arttu Rajantie

Submitted for the degree of Master of Science in

Quantum Fields and Fundamental Forces

September 25, 2020

Abstract

Axions are among the best motivated dark matter candidates. Their isocurvature contribution to the Cosmic Microwave Background is stringently constrained by current measurements, and has so far been evaluated only in the linear approximation. In this Dissertation, we compute the axion isocurvature power spectrum as a mathematical result using the stochastic method, which captures non-linear effects in the axion dynamics. This is done through the evaluation of the axion two-point energy density correlator as a spectral expansion. Finally, the cosmological consequences of our axion model are studied numerically, reproducing results from previous research. Most importantly, the stochastic approach reveals a region with yet unexplored dynamics, having the potential to produce an observable cosmological signature for the axion.

Acknowledgements

I would like to thank my supervisor, Professor Arttu Rajantie, for his invaluable guidance and support throughout the summer. I would also like to thank my family and friends for journeying with me through this exceptional year. G and M, thank you for making lockdown my favourite time at university. A, L, S, and Z, thank you for your encouragement. Isä, thank you for sharing your insights, and finally - Ägä, thank you for sending me to physics.

Contents

1 Introduction

This section motivates the axion through its history (1.2) and its relevance as a dark matter particle (1.1). In addition, the Dissertation aim and method are discussed (1.3), together with a general outline (1.4).

1.1 Dark matter axion

Understanding the fundamental building blocks of the universe lies at the core of theoretical physics. With recent advances in this exploration such as the discovery of the Higgs boson, the visible matter that sustains human existence has been characterised to an incredible accuracy through the Standard Model of particle physics. However, as humbling as it is to modern physicists, the bulk of the Universe's matter remains unknown. The origin of this fundamental substance, named dark matter for obvious reasons, is one of the most profound mysteries of modern physics.

Dark matter is estimated to form 27 % of the Universe's energy, and almost 90 % of its total matter content [1]. With these statistics it is no wonder that enormous experimental and theoretical efforts have been poured into finding this hidden matter since its postulation in the last century. The axion is arguably among the best motivated theoretical particle candidates that could solve this puzzling issue. Its name originates from Nobel laureate Franz Wilczek, who explained in his Nobel lecture in 2004: "I named them [axions] after a laundry detergent, since they clean up a problem with an axial current" [2]. The experimental hunt for axions has been unsuccessful so far. However, a recent excess signal in the Xenon1T experiment looking for dark matter has raised careful hopes in the scientific community that the axion could be detected in the near future [3] (for a preliminary report published in June 2020 the reader is referred to [4]). The validation of this signal would bring axions to the forefront of our current understanding of the Universe, having huge implications on future cosmological research.

1.2 Axion history and motivation

The physics of axions dates back to 1977 when Roberto Peccei and Helen Quinn provided their solution to the strong CP problem [5, 6] by introducing an additional global $U(1)$ symmetry to the Lagrangian of the Standard Model. The spontaneous symmetry breaking of this Peccei-Quinn (PQ) symmetry leads to the postulation of a pseudo-Goldstone boson, the axion, as was first discovered by Weinberg [7] and Wilczek [8]. Even though the axion was originally introduced in the context of solving the strong CP problem, very soon it was noticed that it would be an excellent cold dark matter (CDM) candidate, as it has a low velocity dispersion and weak couplings [2]. The CDM particles predicted by these kinds of invisible axion models are very light and long-lived [2]. Due to this double success of the axion theory in both quantum chromodynamics and cosmology, it is a promising area of research, with a lot of theoretical work done in the past few decades on both conventional QCD axions and axion-like particles (ALPs). The latter ones often arise from theories merging the Standard Model into string theory [9].

Axions can be produced in several ways, such as through the vacuum realignment mechanism [9], which is explored in this Dissertation. The thermal relic axions at the end of inflation would be too hot to model cold dark matter [10], but a CDM axion can also be produced through string and domain-wall decay, which arise as topological defects when the inflation reheat temperature is larger than the temperature scale of the PQ symmetry breaking [2]. However, in this Dissertation we will assume that the PQ symmetry undergoes phase transition during inflation, producing an axion field fluctuating quantum mechanically. The coherent oscillations of this field in the post-inflationary epoch account for the axion CDM particle production.

1.3 Dissertation aim and method

In this Dissertation, the axion two-point energy density correlation function is calculated using the stochastic method, which has previously been done only with the linear approximation. This correlator measuring the axion density fluctuations is then used to evaluate the axion isocurvature power spectrum, since quantum fluctuations in the axion field during inflation cause an isocur-

vature component to the Cosmic Microwave Background (CMB). Finally, these mathematical results are applied to study the cosmological consequences of our axion model in the light of the strict isocurvature bound derived from current observations of the CMB [11].

The two-point correlation function of a scalar field is a physical quantity that characterises perturbations in the field. In cosmology, it is often used in the context of large-scale formation to describe excess probability for galaxies [12], and is measured by experiments such as Planck. In the axion context our two-point correlator incorporates the quantum fluctuations of the axion field during inflation. Mathematically, it is the expectation value of the energy density fluctuations at two spatial points which are asymptotically distant from each other, since we are interested in scales much larger than the Hubble scale, at which particle production occurs.

The stochastic method is used to evaluate this correlator, and is based on dividing the quantum field into a classical and a quantum regime, such that the quantum "kicks" from the short wavelength regime are approximated as stochastic noise, which acts like a random number in the equation of motion of the classical field (see e.g. [13]). Assuming a de Sitter universe during inflation with a constant Hubble parameter H, a Fokker-Planck equation can then be derived for the axion field. This essentially describes the axion field evolution during inflation, giving the probability distribution for the axion field values at the end of the inflationary epoch.

The eigenvalue equation corresponding to this time-dependent Schrödinger-type Fokker-Planck equation is supersymmetric, and is investigated through the Hamiltonian formalism of supersymmetric quantum mechanics. Its eigenspectrum is applied to evaluate the axion two-point correlator as a spectral expansion. In this context we note that all the calculations presented in this Dissertation are evaluated in Mathematica, and natural units are used throughout where both the axion decay constant F_a and the Hubble parameter H are expressed in GeV. The stochastic method avoids the perturbative approach common in axion literature, and reveals a new region between the known free-field limits. Exploring this transition region is the main aim of this Dissertation, together with the analysis of our axion model through its cosmological consequences.

1.4 Dissertation outline

The necessary background to understand the basics of axion physics (2.1) as well as the general stochastic method (2.2) is presented first in Section 2. Section 3 then brings together the key concepts in the evolution of the axion field from the inflationary epoch to its conversion into dark matter particles, involving a detailed discussion on the isocurvature perturbations (3.4).

In Section 4, the stochastic approach for a general scalar field in de Sitter background is introduced, presenting the calculations of the spectral expansion of the two-point correlator (4.3). The interpretation of the stochastic approach in the context of a general scalar field is also discussed (4.2). These results are then applied in Section 5 to the axion field, where its eigenspectrum is studied as a supersymmetric problem (5.2), and the energy dynamics of the axion is investigated through the α parameter (5.3).

Finally, the results are presented in Section 6. These include the mathematical derivation of the axion isocurvature power spectrum (6.1) and its dark matter density parameter (6.2). The values found numerically for the cosmological parameters (the axion decay constant (6.4) and the Hubble parameter (6.5)) are analysed, together with a detailed study on the transition region (6.6), which is a phenomenon revealed by the stochastic approach. This Dissertation then concludes with a discussion on the results in Section 7, highlighting the significance of the stochastic method (7.2), the limitations of our axion model (7.3), as well as its impact on current axion research (7.1).

2 Background

The first part of this section (2.1) highlights how the axion arises as a solution to the strong CP problem, gaining an effective potential that will be important for the stochastic method (see 2.1.3). The general axion is also defined (see 2.1.4). The second part (2.2) introduces the stochastic method, which is the framework used in this Dissertation to calculate the axion correlator.

2.1 QCD axion

2.1.1 $U(1)_A$ symmetry and the strong CP problem

In this subsection, we will follow the conversation in [2] to introduce the strong CP problem and its resolution. In the 1970s it was expected that the strong interaction would be approximately invariant under the $U(2)_{vector} \times U(2)_{axial}$ symmetry. This was due to a larger global symmetry in the quantum chromodynamics (QCD) Lagrangian, in the limit of vanishing quark mass. The $U(2)$ vector symmetry is indeed observed in nature through the conservation of isospin and baryon number. However, the $U(2)$ axial symmetry is broken down spontaneously, as the existence of quark condensates demonstrates. As a result of this spontaneous symmetry breaking, four Goldstone bosons were expected – matching the three pions π_0 and $\pi_\pm$. However, the fourth light hadron state was missing. Steven Weinberg called this the $U(1)_A$ problem and brought forward his assumption that there would be no $U(1)$ axial symmetry in the strong interaction. [2]

It was another Nobel laureate, Gerard 't Hooft, who came up with a solution to this problem. He showed that the structure of the QCD vacuum was more complicated than what was thought at the time. His refined vacuum structure removed $U(1)_A$ as a true symmetry of QCD but introduced a small CP (charge conjugation and parity) violating phase parameter θ associated to the vacuum. The strong CP problem was born: the experimental data suggests that CP is broken only by $\theta \lesssim 10^{-9}$ in QCD. Why is is not badly broken, i.e. why does θ look finetuned? [2]

The more complicated QCD vacuum structure introduced by 't Hooft is based on the axial current of $U(1)_A$, J_5^μ, having a chiral anomaly due to quantum loop corrections. This changes the action

by a pure surface integral [2],

$$\delta S \propto \int d^4x \partial_\mu J_5^\mu \propto \int d^4x G_a^{\mu\nu} \tilde{G}_{a\mu\nu} \, . \tag{2.1}$$

The correct boundary conditions assume a pure gauge field $G^{\mu\nu}$ at infinity, meaning its value is either 0 or some gauge transformation of it. There are gauges for which δS does not vanish. Hence, the action is not invariant under $U(1)_A$ and as Weinberg predicted, $U(1)_A$ is not a symmetry of QCD. Analysing this QCD vacuum structure more carefully, one finds that the true vacuum is actually a superposition of n-vacua [2],

$$|\theta\rangle = \sum_n e^{-in\theta} |n\rangle. \tag{2.2}$$

Furthermore, using the path integral representation for vacuum to vacuum amplitude one can show that the QCD vacuum structure introduces an extra term to the QCD Lagrangian [2],

$$L_\theta = \theta \frac{g_s^2}{32\pi^2} G_a^{\mu\nu} \tilde{G}_{a\mu\nu} \, , \tag{2.3}$$

where G_a is the gluon field strength. This term violates CP, as it conserves charge conjugation but violates parity and time reversal. It also induces a neutron electric dipole moment, which restricts the CP violating phase angle through experimental data to its apparently fine-tuned value $\theta \lesssim 10^{-9}$. [2] So how to resolve the strong CP problem?

2.1.2 Peccei-Quinn solution

The solution proposed by Peccei and Quinn is to extend the Standard Model by an additional chiral (meaning the left and right-handed components are treated differently, thus violating parity by construction) $U(1)$ symmetry, whose role is to effectively counteract the CP violation of the QCD vacuum structure term (2.3). This $U(1)_{PQ}$ symmetry is automatically spontaneously

broken, introducing the axion as its Goldstone boson. [2] The complex scalar field associated to the $U(1)$ Peccei-Quinn symmetry, $\chi(x)$, has two scalar degrees of freedom, $\rho(x)$ and $\phi(x)$, and carries the PQ charge,

$$\chi(x) = \rho(x)e^{i\phi(x)}. \tag{2.4}$$

The PQ symmetry is spontaneously broken at energy scales $\sim F_a$ as $\chi(x)$ has a non-zero vacuum expectation value,

$$\langle\chi(x)\rangle = F_a. \tag{2.5}$$

We can see from Eq. (2.4) that $\phi(x)$ is a dimensionless phase angle. However, we need to scale this field to get the axion field $a(x)$, which has the canonical kinetic term. Using Eq. (2.5),

$$a(x) = F_a\phi(x), \tag{2.6}$$

where F_a is the decay constant of the axion, setting both the strength of the axion interactions, as well as the periodicity of the axion potential. We will assume in this Dissertation that F_a is constant, but we note that scenarios with a dynamical decay constant have been studied (see e.g. [14]). According to classical field theory, after the spontaneous symmetry breaking (SSB) the radial $\rho(x)$ is set to the vev (2.5). The other degree of freedom, the axion (2.6), is the Goldstone mode that remains massless. Finally, we note that under a $U(1)_{PQ}$ transformation,

$$a(x) \to a(x) + \omega F_a, \tag{2.7}$$

where ω parametrises the transformation.

2.1.3 Effective potential

The axion field has an effective potential, which can be derived from the total $U(1)_{PQ}$ invariant Lagrangian that brings together the axion and the QCD theory [2],

$$L_{\text{total}} = L_{\text{SM}} + \theta \frac{g_s^2}{32\pi^2} G_c^{\mu\nu} \tilde{G}_{c\mu\nu} - \frac{1}{2}\partial_\mu a \partial^\mu a + L_{\text{int}}\left[\frac{\partial^\mu a}{F_a}, \psi\right] - \frac{a}{F_a}\frac{g_s^2}{32\pi^2} G_c^{\mu\nu} \tilde{G}_{c\mu\nu}. \tag{2.8}$$

Due to the SSB of $U(1)_{PQ}$, we have $a(x)$ instead of $\chi(x)$. The first term on the right hand side of Eq. (2.8) is the Standard Model (SM) Lagrangian, followed by the QCD vacuum structure term (2.3), the axion kinetic term, and the axion-SM particle interaction term. The last term of Eq. (2.8) is the chiral anomaly term of the $U(1)_{PQ}$ symmetry, which is directly analogous to the QCD vacuum term (2.3). If $U(1)_{PQ}$ was broken only spontaneously, the axion would indeed be a massless degree of freedom (see section 2.1.2). However, this chiral anomaly term explicitly breaks $U(1)_{PQ}$ [2]. Its physical consequence is that $a(x)$ is actually a pseudo-Goldstone mode with a small mass. In addition, its interaction with the corresponding QCD vacuum term (2.3) produces a potential for $a(x)$, which goes as a cosine in the effective vacuum angle [2],

$$V_{\text{eff}} \sim \cos\left(\frac{a(x)}{F_a} - \theta\right). \tag{2.9}$$

Hence, the effective CP violating phase is not the static QCD θ anymore, but the dynamical $\frac{a(x)}{F_a} - \theta$, combining all the CP violation of the Lagrangian [2], and eventually reaching 0 when the axion field reaches the minimum of the potential (2.9) at

$$\langle a \rangle = \theta F_a. \tag{2.10}$$

At the minimum of this effective potential, the CP violation in the axion field cancels that from QCD theory. This can directly be seen from the total Lagrangian (2.8), as setting the axion field

to its vev (2.10) makes the two chiral anomaly terms in L_{total} cancel. [2] Therefore, when the axion field is in its vacuum state, the theory predicts no CP violation, while small deviations from it introduce a vanishing CP violating parameter, which is consistent with experiments [10].

Since the QCD CP violating phase θ is static, in the following calculations we can just shift the potential to cancel it, and this is indeed done in most of the literature on axion fields (see e.g. [15]). Then the effective potential will have the final form

$$V(a) = V_0\left[1 - \cos\left(\frac{a}{F_a}\right)\right], \tag{2.11}$$

and no CP violation corresponds to the minimum of this potential at $a(x) = 0$. This potential (2.11) for the axion field is the one that is used in this Dissertation to calculate the axion correlator (see Section 5.1). It has a period of 2π in the dimensionless parameter ϕ (recall (2.6)). Therefore, all of the calculations in this Dissertation will be done across a range $[-\pi, \pi]$ in this dimensionless phase angle.

The amplitude of the potential (2.11), V_0, is evaluated from field theory as $V_0 = F_a^2 m_a(T)^2$ (see e.g. [16]), where $m_a(T)$ is the mass the axion acquires through the explicit symmetry breaking of $U(1)_{PQ}$. This mass depends on the temperature of the universe close to the QCD breaking scale, but later acquires an asymptotic zero temperature value [16]. It is generally characterised through the topological susceptibility of QCD, $\chi(T)$, which enables to write the mass as $m_a(T) = \chi(T)m_a^2(T = 0)$ [17]. Here $m_a(T = 0)$ is the asymptotic zero mass. For detailed calculations on the axion mass using the QCD topological susceptibility, the reader is referred to [18]. We note that as QCD is highly non-perturbative, the temperature dependence of the axion mass is best evaluated using lattice QCD (see e.g. [19]).

In this Dissertation, we are interested in the final axion energy density correlator, which is evaluated after the end of inflation when the axion field has rolled down to its minimum. Therefore, we assume that the universe has radically cooled down at that point compared to inflationary

temperature scales, so the asymptotic zero mass limit holds. Thus, in this Dissertation we will assume a constant axion mass. In this context we also note that in axion literature it is commonly stated that the axion acquires its mass and its effective potential only at the QCD breaking scale Λ_{QCD} (see e.g. [16]). However, this statement includes the assumption that the inflationary Hubble parameter H_I, which is related to the axion energy density, is dominating during inflation compared to the axion potential, and the axion can be treated as a massless free field (see Section 5.3.1). Hence, the mass would "turn on" only when the axion potential becomes important relative to the Hubble parameter. However, as QCD effects and instantons exist at all times during inflation, we will assume the axion acquires its effective potential and a mass already at the PQ phase transition. This is also required by the stochastic method, which uses the axion potential as one input to characterise the quantum field (see Section 5.1).

2.1.4 General axion

For the rest of this Dissertation, we make an important distinction between the conventional axion arising from pure QCD theory presented in Section 2.1, which we call from now on the QCD axion, and a general axion that can originate from other Standard Model extensions or from string theory, for example (see [20]). In our calculations, the QCD and general axion will differ by the amplitude V_0 of their potential. While the QCD axion has its potential bound by

$$V_0 \simeq \Lambda_{QCD}^4, \tag{2.12}$$

where Λ_{QCD} is the QCD breaking scale ~ 250 MeV [21], we assume no such bound on V_0 for the general axion. For completeness we note that Eq. (2.12) implies $m_a \approx \frac{\Lambda_{QCD}^2}{F_a}$ [13] for the asymptotic zero mass of the QCD axion. In this Dissertation, only this mass will be evaluated, and hence the mass will always implicitly refer to the QCD axion.

2.2 Stochastic method and the Fokker-Planck equation

2.2.1 Basics of stochastic processes

Stochastic processes are random processes, where one or multiple variables have an inherently random probability distribution, or they are analysed statistically as such as the system itself would be too complicated to be solved deterministically. The most famous example is Brownian motion, where in theory one could solve the set of coupled differential equations arising from the motion of every single particle in the system and thus find deterministic equations of motion. However, in view of the size of the system, the stochastic approach provides a powerful tool to analyse the motion of the particles through probabilistic quantities.

The Fokker-Planck (F-P) equation was first applied exactly in this context, introducing random fluctuations to an otherwise deterministic system. For Brownian motion, those fluctuations represent random momentum kicks to the particles in the system. These particles then have a probability distribution from which different quantities, such as their average location, can be calculated [22]. The Fokker-Planck equation is a differential equation for this probability density function (PDF) of the system. More generally, the Fokker-Planck equation provides an equation of motion for the distribution function of macroscopic variables in the system which exhibit fluctuations near transition points, where the transition from one state to another can be treated as a random (and often microscopic) process [22]. In the context of this Dissertation, the transition point is the wavelength that divides the axion scalar field modes into the classical (macroscopic) and the quantum (microscopic) regimes (see Section 4.1). Solving the Fokker-Planck equation gives the probabilistic time evolution of the system. Its solutions are generally quite difficult to find, but even if analytic solutions do not exist, several numerical methods such as the simulation method, numerical integration and the eigenfunction expansion can be used [22]. The latter is the method used for calculations in this Dissertation, and is presented in detail for the actual axion scalar field in Section 5.

2.2.2 Langevin equation

The Fokker-Planck equation often arises from a stochastic Langevin equation. Its basic form is [23],

$$\dot{x} + \beta(x) = f(t), \tag{2.13}$$

where $x(t)$ is the stochastic quantity of which the PDF needs to be solved with the F-P equation. The $\beta(x)$ term represents a potential for the stochastic quantity, and it is derived from the macroscopic theory. On the other hand, the stochastic noise term $f(t)$ represents the microscopic (inherently) random theory, which in the case of this Dissertation is the quantum world. Hence, the Langevin equation combines the microscopic and macroscopic parts of a system into one stochastic equation, where the macroscopic theory gets a random "kick" and thus its statistical properties such as its PDF and correlation function can be considered. [23]

The F-P equation can be derived from the stochastic Langevin equation in multiple different ways, see [22] for several in-depth derivations using for example the Kramers-Moyal expansion. A simplified, yet mathematically debatable derivation can be found in [23], which relies on finding the first and second moment of the PDF in two ways, directly from the probability theory and by integrating the Langevin equation. This method makes use of the first two derivatives of the Dirac delta function. The first derivative introduces a drift in the density distribution, while the second derivative of the Dirac delta brings diffusive broadening to the PDF [23]. Hence, the derivation shows explicitly how the F-P equation captures the diffusive spread and drift of the PDF of a macroscopic variable, which is influenced by the potential and the random noise term as introduced in the Langevin equation (2.13).

2.2.3 General Fokker-Planck equation

The general form of the Fokker-Planck equation is (as derived in [23])

$$\frac{\partial \rho(x,t)}{\partial t} = \frac{\partial}{\partial x}\big[\beta(x)\rho(x,t)\big] + D\frac{\partial^2 \rho(x,t)}{\partial x^2}, \tag{2.14}$$

where $\rho(x,t)$ is the PDF of the stochastic quantity x, $\beta(x)$ is the potential as given in Equation (2.13), and D is a diffusion coefficient associated with the stochastic noise term $f(t)$, which is assumed to be constant [23]. By integrating the PDF solved from the F-P equation, the expectation value of any function of the stochastic quantity x can be determined [24],

$$\langle F(x,t)\rangle = \int dx F(x)\rho(x,t). \tag{2.15}$$

Several key properties of the stochastic noise term $f(t)$ (see Eq. (2.13)) in the context of this Dissertation are worth mentioning. It is assumed to be a Gaussian white noise term, i.e. its correlation function is proportional to a Dirac delta, where white refers to a spectral distribution independent of the frequency [22]. Its correlation function is generally given by [22]

$$\langle f(t)f(t')\rangle = 2D\delta(t-t'), \tag{2.16}$$

where D is both the amplitude of the noise and the diffusion coefficient entering the F-P equation (2.14). The Markoff condition states that the value of $f(t)$ is uncorrelated between different time intervals [23], which is in line with $f(t)$ acting like a random number generator.

3 Axion field evolution

This section covers the evolution of the axion field from its creation during inflation to particle production through the realignment mechanism (3.1-3.2). The axion energy density function (3.3) and isocurvature perturbations (3.4) are explored in detail.

3.1 Vacuum realignment mechanism

In this Dissertation we assume that the PQ phase transition, during which the axion field is generated (see Section 2.1.2), occurs during inflation. The axion field then undergoes quantum fluctuations until the end of inflation, in the same way as the inflaton. Both are massless and weakly-coupled, hence they share a similar fluctuation spectrum. [2] At the end of inflation, the axion field "freezes out" to a different value in each Hubble volume, called the misalignment angle [2]. If we assume that $\phi = 0$ corresponds to the vacuum, where there is no CP violation, the misalignment angle can be any in the range $[-\pi, \pi]$, and corresponds to an offset of the field from its minimum, along the axion effective potential (2.11).

The probability distribution for the misalignment angle is given by the stochastic method (see Section 2.2), which we use to calculate the axion density correlator. Using (2.6), we write the axion field value in each Hubble volume as $a = F_a\phi_{\text{mis}}$, where ϕ_{mis} is the misalignment angle. For the rest of this Dissertation, we will not denote this explicitly, as all the calculations are related to the post-inflationary epoch where the axion field has acquired this value. In the stochastic approach, integrating over ϕ is thus equivalent to integrating over the possible misalignment angles. Often in literature it is assumed that the axion field would be homogeneous in the whole observable universe, taking on a single value that defines its energy density (see e.g. [2, 25]). However, this generalisation is avoided with our stochastic method, which works with a probability distribution.

After the freeze-out at the end of inflation, the axion field will eventually start oscillating around the minimum of its potential, once the slow-roll condition is not valid anymore [26]. These oscillations are the mechanism for particle production, called vacuum realignment [26], where the

energy of the axion field is converted into particles behaving as cold dark matter (CDM). Figure 1 brings together the most important events in the axion field evolution.

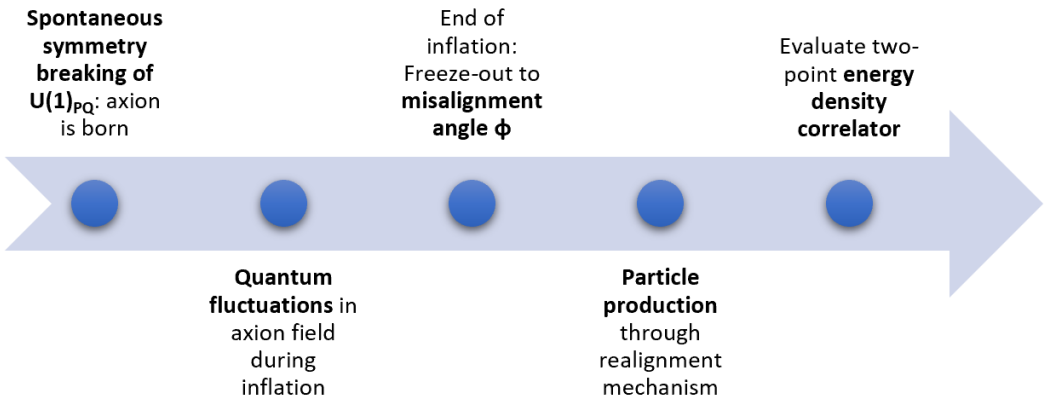

Figure 1: The main events in the axion field evolution from the spontaneous symmetry breaking of the PQ symmetry until the present day, when we want to evaluate the axion density correlator.

3.2 Equation of motion and Hubble friction

The equation of motion of the axion field after the freeze-out determines how the axion particles are born from the oscillations of the field. The general form can be written as [27]

$$\ddot{a} + 3H\dot{a} + V'(a) = 0, \tag{3.1}$$

where the prime denotes a derivative with respect to the field $a(x)$. In the quadratic approximation this becomes the equation for a damped harmonic oscillator with $V'(a) \approx m_a^2 a$ [17]. The Hubble parameter H quantising the expansion of the universe introduces Hubble friction in the field evolution, through the second term in (3.1) [17]. Therefore, if the axion field value due to the misalignment is close to $\pm\pi$, it will stay constant for a long time. On the other hand, the last term in Eq. (3.1) with the derivative of the potential is the gradient force that pulls the axion field towards the minimum.

When these two counteracting terms reach the same order of magnitude ($m_a \sim 3H$), the Hubble friction becomes too weak and the axion field will start rolling down towards the minimum of the potential [28]. As we assume a constant mass for our axion theory, this will happen due to the decrease of the Hubble parameter as the universe cools down. Since particle production is due to the oscillations about the minimum, more particles are produced if the field is initially closer to the top of the potential, as the oscillations will have a larger amplitude and last longer. Hence, the final axion energy density depends strongly on the initial misalignment angle.

3.3 Interpolating the energy density function

To capture this dependence of the final axion energy density on the misalignment angle, we need to find a function that encodes the information on how the energy in the axion field is converted into particles through the realignment mechanism. This function contains a logarithmic part that can be derived directly from the equation of motion of the axion field (3.1). We also know that when the amplitude of the axion field oscillations becomes small enough ($\phi \ll 1$), the axion potential (2.11) can be approximated as quadratic. The axions then behave as free massive particles whose behaviour can be approximated as a harmonic oscillator (see Section 5.3.1). The energy density in these small oscillations can be approximated as [15]

$$f_{\text{harm}}(\phi) = \frac{1}{2} m_a^2 F_a^2 \phi^2 \,. \tag{3.2}$$

Most of the current research on axions uses this quadratic approximation for the axion density. We want to combine the logarithmic part (presented e.g. in [10]) with the harmonic behaviour at the bottom of the potential. Several candidates for the axion energy density are represented in Figure 2, with the quadratic approximation in red. The logarithmic factor entering the yellow and green candidates is a common anharmonic factor (see e.g. [29]), producing a divergence at $\phi = \pm\pi$, and is multiplied by a quadratic part dominating at low values of the misalignment angle. For the calculations in this Dissertation, we choose to use the simplest density function,

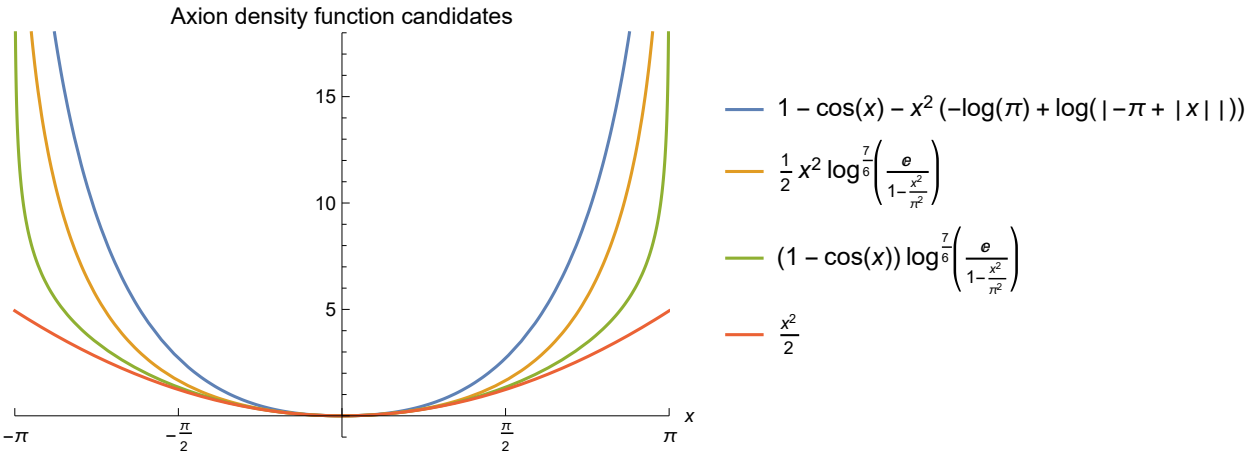

Figure 2: The axion density function candidates (without the dimensional factor $m_a^2 F_a^2$), and the quadratic approximation (in red).

in yellow, and multiplying it with the correct constants $m_a^2 F_a^2$ by dimensional analysis, we get

$$f_{\text{full}}(\phi) = m_a^2 F_a^2 \frac{\phi^2}{2}\left[\ln \frac{e}{1-\frac{\phi^2}{\pi^2}}\right]^{\frac{7}{6}}. \tag{3.3}$$

This function gives the final energy density of the axion field in each Hubble volume, as a function of the misalignment angle, after the axion particles have been created. In the low ϕ limit, we recover the quadratic approximation given in Eq. (3.2), as is seen from Fig. 2 where our function (in yellow) aligns itself with the harmonic function (in red). Finally we note that in the ideal case, the axion density function would be periodic over the $[-\pi, \pi]$ range, as ϕ is a phase angle that is periodic over 2π. However, since the axion correlator requires an integration over one period only, we do not need to modify this interpolated density function to account for the periodicity.

3.4 Isocurvature perturbations

Quantum fluctuations of the inflaton scalar field during inflation produce curvature fluctuations that are the main cause for the temperature anisotropies of the Cosmic Microwave Background (CMB) [30]. These density perturbations in matter are called "adiabatic", and they satisfy [30]

$$\frac{\delta\rho_{matter}}{\rho_{matter}} = \frac{3}{4}\frac{\delta\rho_{rad}}{\rho_{rad}} \,. \tag{3.4}$$

However, just as the inflaton, the massless and weakly-coupled scalar axion field undergoes similar fluctuations during the inflationary epoch [2]. These cause dark matter density perturbations, as the axions born through the realignment mechanism are themselves CDM particles. Quantum mechanical fluctuation contributions to the CMB anisotropies from other scalar fields than the inflaton are generally named "isocurvature" perturbations [2]. The adiabatic and isocurvature components are usually assumed to be uncorrelated [16].

The existence of any non-adiabatic fluctuations, changing the relation between the matter and radiation spectrum, is an indication of the presence of other scalar fields than the inflaton in the inflationary epoch [30]. Hence, postulating the axion field introduces an isocurvature contribution to the CMB anisotropies [31], arising from the role of the axionic dark matter in the total energy density of the universe. The current data from the CMB constrains the isocurvature contribution radically [32]. Therefore, the isocurvature component predicted by the axion model must be small enough to fit this experimental bound. This theoretical axion contribution is what this Dissertation aims to evaluate, with the help of the stochastic method. Results falling just below the current observational limit are particularly interesting, as in the future more accurate CMB observations will be able to place stricter bounds.

Two things must be noted in the context of axion isocurvature perturbations. Firstly, if the PQ symmetry is broken after inflation (not the scenario considered in this Dissertation), axion models still produce an isocurvature component but it acts on length scales similar to the QCD horizon, which is much smaller than the CMB scale. While these perturbations cannot be observed in the CMB spectrum, they lead to new phenomena such as axion miniclusters. [2] Secondly, while we are assuming that the radial part of the complex PQ field is at its vev (Eq. (2.5)), a high inflation scale may cause QM fluctuations also in this radial part that might restore the PQ symmetry, and hence erase isocurvature perturbations [16].

4 Stochastic approach for a general scalar field

This section applies the stochastic method introduced in Section 2.2 to a general scalar field (4.1), demonstrating how to calculate the spectral expansion of its two-point correlator (4.3). A discussion on the interpretation of the stochastic method in this context is also included (4.2).

The stochastic approach in an inflationary context has been studied e.g. in [33], with Starobinsky and Yokoyama introducing its application to a self-interacting scalar field in de Sitter background [24], for both a free field and a minimally coupled $\frac{1}{4}\lambda\phi^4$ theory. The same method has later been implemented for several types of potentials, such as a double-well potential (see [34]). In this Dissertation, we will apply it to the axion potential (2.11).

The main goal in the use of the stochastic approach for a scalar field is to find its one-point equilibrium probability distribution using the Fokker-Planck equation, from which important quantities such as the two-point correlator of an arbitrary local function of the field can be calculated as a spectral expansion [35] (see [36, 37, 38] for examples of scalar field correlators in de Sitter background). We compute this correlator for the energy density of the axion field in this Dissertation, as it allows to evaluate the power spectrum of the axionic isocurvature perturbations (see Section 6.1). It is worth noting that while the use of the one-point probability distribution is common, the stochastic approach for correlators has been overall less studied [35].

In the following, the axion field is assumed to a be a spectator field, i.e. a light scalar field that develops superhorizon ($\lambda > \frac{1}{H}$) fluctuations during the inflationary epoch [35]. The stochastic approach for a spectator field (see e.g. [39, 40]) takes into account the axion self-interactions in the early universe, which are apparent from the non-harmonicity of the axion potential. However, in this Dissertation we ignore the axion self-interactions of the present day. For more detail on spectator field self-interactions, the reader is referred to [41]. Finally, we note that for the general discussion in this section, the symbol ϕ refers to an arbitrary scalar field, which would correspond to $a(x)$ for the axion field.

4.1 Langevin equation of the coarse-grained field

The main steps in [24] that are applicable to the case of the axion scalar field are reviewed below. Writing the Heisenberg operator of the quantum field $\hat{\phi}$ as

$$\hat{\phi}(\vec{x},t) = \bar{\phi}(\vec{x},t) + \int \frac{d^3k}{(2\pi)^{\frac{3}{2}}}\theta\big(k - a(t)H\big)\Big[\hat{a_k}\phi_k(t)e^{-i\vec{k}\cdot\vec{x}} + \hat{a_k}^{\dagger}\phi_k^*(t)e^{i\vec{k}\cdot\vec{x}}\Big], \tag{4.1}$$

the quantum field can be split into two regimes: the long wavelength (classical) regime represented by $\bar{\phi}(\vec{x},t)$, also called "coarse-grained" field, and the short wavelength (quantum) regime which has the familiar form of a quantum field with the creation and annihilation operators. $H = \frac{\dot{a}}{a}$ is the Hubble parameter, which is assumed constant to keep the equation as simple as possible, and $a(t)$ is the scale factor. As mentioned in section 2.2.1, the stochastic approach is often used near transition points. In this case, the transition point is the wavelength that divides the modes of the quantum field into these two regimes, and is implemented by the step-function $\theta\big(k - a(t)H\big)$ in Eq. (4.1). Hence, the modes with $k > a(t)H$ belong to the quantum regime, whereas wavelengths longer than the Hubble horizon are treated classically in this sharp cut-off approximation.

By varying the action of the scalar field in de Sitter space, one can find the equation of motion for the short wavelength part, approximating it as a free field, which can be solved analytically (see [24]). The action for the axion field using the dimensionless $\phi(x)$ (2.6) can be written as [25]

$$S_\phi = \int d^4x\sqrt{-g}F_a^2\Big[-\frac{1}{2}\nabla_\mu\phi\nabla^\mu\phi - V(\phi)\Big], \tag{4.2}$$

where $V(\phi) = m_a^2(1-\cos\phi)$ and g is the determinant of the FLRW metric.

In this Dissertation, we concentrate on the coarse-grained field, since the regime of interest for calculating the two-point correlator at asymptotic distances is the super-horizon scale. Hence, in the method presented in this Dissertation, the resulting Fokker-Planck equation will be an equation for the probability distribution of the classical long wavelength part, ignoring the micro-

scopic degrees of freedom. Starting again with the de Sitter action (Eq. (4.2) for the axion field), the equation of motion for the coarse-grained field $\bar{\phi}(\vec{x},t)$ can be computed to find the classical equation [24],

$$\dot{\bar{\phi}}(\vec{x},t) = -\frac{1}{3H}V'(\bar{\phi}) + f(\vec{x},t), \tag{4.3}$$

where prime gives the derivative with respect to ϕ, and $V(\phi)$ is the potential of the scalar field. To derive this equation, several assumptions have been made. Firstly, the derivatives of the field are taken to be small at long distances, i.e. $\nabla^2\phi \approx 0$ compared to the other terms. This is the equivalent condition to slow-roll for the inflaton. Secondly, the system is assumed to be overdamped, i.e. $\ddot{\bar{\phi}} \approx 0$. The term $f(\vec{x},t)$ in (4.3) is given by [24]

$$f(\vec{x},t) = a(t)H^2 \int \frac{d^3k}{(2\pi)^{\frac{3}{2}}}\delta\big(k - a(t)H\big)\Big[a_k\phi_k(t)e^{-i\vec{k}\cdot\vec{x}} + a_k^\dagger\phi_k^*(t)e^{i\vec{k}\cdot\vec{x}}\Big]. \tag{4.4}$$

Tying this back to the general stochastic method presented in Section 2.2, we notice that the classical equation of motion (4.3) is a Langevin equation for the stochastic field $\bar{\phi}$ (compare with Eq. (2.13)). The role of $\bar{\phi}$ as an operator does not affect the stochastic treatment [24]. $f(\vec{x},t)$, given by Eq. (4.4), plays the role of the stochastic noise term in Eq. (2.13). It arises from the interaction of the quantum and classical parts of the original quantum field, representing a quantum regime contribution entering the classical equation of motion (4.3) due to the expansion of the universe. This is important: why do we find a stochastic Langevin equation by solving the equation of motion for the classical field? From where does the randomness come into play?

4.2 Interpreting the stochastic approach and the Fokker-Planck equation

From a physical point of view, the short wavelength part of the scalar field contains the quantum modes, and the Hubble horizon marks the transition point to the classical regime. However, as the universe expands, each Fourier mode that was once in the quantum regime will move into the classical one due to its stretching by the expansion. This transition is the stochastic noise captured by $f(\vec{x},t)$ (4.4). If the universe would not be expanding, the quantum modes would stay in the quantum regime, and thus no noise would be introduced into the system. To deal with this stochastic noise term, we first treat it normally as a quantum field operator and calculate its quantum two-point correlation function, which is given by [24]

$$\langle f(\vec{x},t_1)f(\vec{x},t_2)\rangle = \frac{H^3}{4\pi^2}\delta(t_1-t_2), \tag{4.5}$$

where we concentrate on the time correlator, i.e. we set $\vec{x_1} = \vec{x_2} = \vec{x}$. Comparing Eq. (4.5) to the general white noise term (2.16), we see that $f(\vec{x},t)$ is indeed a white noise term, as its correlator is proportional to the Dirac delta function. The conceptual mathematical jump from this purely quantum theory derived equation (4.5) is to approximate the quantum term $f(\vec{x},t)$ in the stochastic Langevin equation (4.3) as a random number, whose value is determined by the probability distribution of a classical field that would have the two-point correlator (4.5). Hence, we are approximating the $f(\vec{x},t)$ quantum field (4.4) as a classical field, whose correlator properties are determined from quantum theory, and the mathematical effect of this stochastic noise term is a random number entering the equation of motion (4.3).

Physically, this random number represents a "quantum kick" of a QM mode transitioning from the quantum regime into the classical one. In the case of a scalar field in an expanding de Sitter background, we can think of "doing a measurement" every time the field transverses the Hubble horizon, our transition point, i.e. one quantum mode joins the classical field. The amplitude of this kick is approximated as a random number, as QM theory is inherently probabilistic. The measurement gives the value of any observable of the quantum field, and in our case we are

interested in the two-point correlation function, hence we use the PDF of the quantum two-point correlator (4.5) to evaluate our stochastic noise term.

It is worth noting at this point that while Brownian motion is inherently deterministic, and the stochastic approach is a computationally feasible way to treat a Brownian system, as introduced in Section 2.2.1, the Langevin equation (4.3) arising in the context of a scalar field is inherently stochastic, as it contains the quantum regime modes that are non-deterministic by nature. Hence, approximating them with a stochastic noise term following the PDF derived from quantum theory is a physically valid method for finding the correlation functions.

Finally, as introduced in section 2.2.3, the Fokker-Planck equation for the one-point probability distribution of $\bar{\phi}$ can be derived from the Langevin equation, and is given by [24]

$$\frac{\partial \rho_1[\phi]}{\partial t} = \frac{1}{3H}\frac{\partial}{\partial \phi}\{V'[\phi]\rho_1[\phi]\} + \frac{H^3}{8\pi^2}\frac{\partial^2 \rho_1[\phi]}{\partial \phi^2}, \tag{4.6}$$

where the diffusion coefficient $D = \frac{H^3}{8\pi^2}$ comes from comparing the general white noise term in Eq. (2.16) with our quantum correlator (4.5). This Fokker-Planck equation is deterministic, as all the randomness has been integrated away from the Langevin equation. Another important property is that it is linear. Hence, a spectral expansion can be used to determine the two-point correlation function, which is presented in the next section.

4.3 Spectral expansion of the two-point correlator

4.3.1 General two-point correlator

The following calculations will use the approach taken by [35]. We make the assumptions that the two-point correlator is evaluated at super-horizon scales ($\lambda \gg \frac{1}{H}$), the field is light ($V''(\phi) < H$) and energetically subdominant. The aim of the spectral expansion method presented in this section is to find the two-point correlator of a general function $f(\phi)$. This has the form [35]

$$G_f(t_1, t_2; \vec{r_1}, \vec{r_2}) = \langle f(\phi(t_1, \vec{r_1}))f(\phi(t_2, \vec{r_2}))\rangle, \tag{4.7}$$

so it is an expectation value of the function. However, as we assume a de Sitter background, and we are interested in the correlator at asymptotically far distances, de Sitter invariance can be invoked to make the calculations easier. Just as in Minkowski space the scalar quantities are only dependent on ds^2, in the maximally symmetric de Sitter space the correlator of a de Sitter scalar observable can only be dependent on the de Sitter invariant quantity [35],

$$y = \cosh\big(H(t_1 - t_2)\big) - \frac{H^2}{2}e^{H(t_1+t_2)}|\vec{r_1} - \vec{r_2}|^2. \tag{4.8}$$

Hence, we can first evaluate the temporal two-point correlator (defined by $|\vec{r_1} - \vec{r_2}| = 0$), which is relatively straightforward, and later rotate it in de Sitter space to the spatial correlation function (defined by $|t_1 - t_2| = 0$), which is the correlator we want to compute as it captures the correlation of axion density fluctuations between spatially separated points (see Section 4.3.4). We note that this rotation requires an analytical extension to negative values, but below we only state the key results. Assuming asymptotically large time- and space-like separations, the general correlator can be expressed as [35]

$$G_f(t_1, t_2; \vec{r_1}, \vec{r_2}) = G_f(H^{-1}\ln|2y - 1|), \tag{4.9}$$

where the right hand side corresponds to the temporal correlation function [35],

$$G_f(t;0) = \langle f(\phi(t))f(\phi(0))\rangle. \tag{4.10}$$

In our treatment, the general scalar field $\phi(x)$ is the axion field $a(x)$ and $f(\phi)$ is its final energy density f_{full} (3.3) which we found in Section 3.3. It is important to note that asymptotically long distances (i.e. $|\vec{r_1} - \vec{r_2}| \gg 1$) in the spatial correlator correspond to $|t_1 - t_2| \gg 1$ in the temporal correlator.

4.3.2 Schrödinger-type eigenvalue equation

Starting from the Langevin equation for the coarse-grained field (4.3), its corresponding Fokker-Planck equation (4.6) can be written in the form of a Schrödinger-type equation [35],

$$\frac{\partial P(t;\phi)}{\partial t} = D_\phi P(t;\phi). \tag{4.11}$$

Here $P(t;\phi)$ is the one-point PDF that obeys the Fokker-Planck equation, giving the probability distribution for the value of the field ϕ at a given time t. D_ϕ is the operator [35]

$$D_\phi \equiv \frac{1}{3H}\left[V''(\phi) + V'(\phi)\frac{\partial}{\partial\phi}\right] + \frac{H^3}{8\pi^2}\frac{\partial^2}{\partial\phi^2}, \tag{4.12}$$

where the coefficient of the last term comes from the amplitude of the stochastic noise term in the Langevin equation (4.3). To find the equilibrium distribution of $P(t;\phi)$, we set $\frac{\partial P}{\partial t} = 0$ from which one can see that [35]

$$P_{eq} \propto e^{-\frac{8\pi^2}{3H^4}V(\phi)}. \tag{4.13}$$

Through this equilibrium distribution (4.13) we observe how the Hubble parameter H comes into play, bringing in the theory the fact that the universe is expanding. In the axion context, if H is really small, the probability distribution will give a sharp Gaussian centred at the minimum of the axion potential, and hence the axion field will oscillate near the bottom (no expansion would imply no oscillations). On the other hand, for large H (significant expansion of the universe) P_{eq} approaches a uniform distribution, i.e. it is equally likely for the axion field value at the end of inflation to be near the top of the potential than at the bottom. The reason H is such an important parameter in our stochastic theory is that we can link it to the energy density of the field, which in turn determines how freely the axion can move in its potential.

As shown in [35], which follows the approach of Starobinsky and Yokoyama [24], defining

$$\tilde{P}(t,\phi) = e^{\frac{4\pi^2 V(\phi)}{3H^4}} P(t,\phi), \tag{4.14}$$

Eq. (4.11) becomes

$$\frac{\partial \tilde{P}(t;\phi)}{\partial t} = \frac{3H^3}{4\pi^2} \tilde{D}_\phi \tilde{P}(t;\phi), \tag{4.15}$$

where

$$\tilde{D}_\phi = \frac{1}{2}\frac{\partial^2}{\partial \phi^2} - \frac{1}{2}\big(v'(\phi)^2 - v''(\phi)\big) \quad \text{and} \quad v(\phi) = \frac{4\pi^2}{3H^4} V(\phi). \tag{4.16}$$

As equation (4.15) is linear, separation of variables can be used to find independent solutions of the form

$$\tilde{P}_n(t;\phi) = e^{-\Lambda_n t} \psi_n(\phi), \tag{4.17}$$

where $\psi_n(\phi)$ obeys a time-independent Schrödinger-type eigenvalue equation,

$$\tilde{D}_\phi \psi_n(\phi) = -\frac{4\pi^2 \Lambda_n}{H^3} \psi_n(\phi), \tag{4.18}$$

where the eigenfunctions $\psi_n(\phi)$ are assumed to be both orthonormal and complete. One can also show (see [24]) that $\Lambda_n \geq 0$. It can easily be seen that a stationary solution exists, i.e. the lowest eigenvalue is $\Lambda_0 = 0$, and by comparing with Eq. (4.13) one finds that [35]

$$P_{eq}(\phi) = \psi_0(\phi)^2. \tag{4.19}$$

4.3.3 Spectral expansion method

In this subsection we follow the approach in [35]. To derive the spectral expansion of the temporal two-point correlation function, one can make use of the linearity of the probability distributions between different times which is clear from the transfer matrix $\tilde{U}(\Delta t; \phi, \phi_0)$,

$$\tilde{P}(t + \Delta t; \phi) = \int d\phi_0 \tilde{U}(\Delta t; \phi, \phi_0) \tilde{P}(t; \phi_0), \tag{4.20}$$

where $\tilde{U}(\Delta t; \phi, \phi_0)$ obeys the same differential equation (4.15) as $\tilde{P}$. The unscaled probability distribution can be written based on (4.20) as

$$P(t + \Delta t; \phi) = \int d\phi_0 e^{-\frac{4\pi^2}{3H^4} V(\phi)} \tilde{U}(\Delta t; \phi, \phi_0) e^{\frac{4\pi^2}{3H^4} V(\phi_0)} P(t; \phi_0), \tag{4.21}$$

and we can write the transfer matrix entering (4.20) as a spectral expansion using the eigenfunctions from Eq. (4.18) (see [35] for a more careful analysis),

$$\tilde{U}(t;\phi,\phi_0) = \sum_n e^{-\Lambda_n t}\psi_n(\phi)\psi_n(\phi_0). \tag{4.22}$$

Now, as the two-point correlator is an expectation value, its basic form is

$$G_f(t) = \langle f(\phi_0)f(\phi(t))\rangle = \int d\phi f(\phi_0)f(\phi)P(t;\phi), \tag{4.23}$$

where one must integrate over the field ϕ weighted by the PDF of the one-point function of the field, $P(t;\phi)$, defined from Eq. (4.11). For evaluating $P(t;\phi)$ in Eq. (4.23), we use Eq. (4.21) with $t = 0$, $\Delta t = t$, and $P(0;\phi_0) = P_{eq}(\phi_0)$. Furthermore, using (4.19), and noticing that

$$e^{\frac{4\pi^2}{3H^4}(V(\phi_0)-V(\phi))}\psi_0(\phi_0) = \psi_0(\phi), \tag{4.24}$$

the correlator $G_f(t)$ from Eq. (4.23) takes the form [35]

$$G_f(t) = \int d\phi \int d\phi_0 f(\phi_0)f(\phi)\psi_0(\phi_0)\tilde{U}(t;\phi,\phi_0)\psi_0(\phi). \tag{4.25}$$

Finally, substituting in the spectral expansion of the transfer matrix (4.22),

$$G_f(t) = \sum_n \langle 0|f|n\rangle\langle n|f|0\rangle e^{-\Lambda_n t} = \sum_n f_n^2 e^{-\Lambda_n t}, \tag{4.26}$$

we find the final form of the spectral expansion of the two-point correlator of a function $f(\phi)$, where the spectral coefficient is written in Dirac notation,

$$f_n = \langle 0|f|n\rangle = \int d\phi \psi_0(\phi)f(\phi)\psi_n(\phi). \tag{4.27}$$

It is worth noting that if the original potential $V(\phi)$ entering the eigenvalue equation (4.18) has a symmetry, this propagates to the eigenfunctions, which will affect strongly the spectral coefficients (4.27) if $f(\phi)$ has parity [35]. The integration range of (4.27) is $[-\pi, \pi]$ in the dimensionless ϕ for the axion case, as the axion potential is periodic.

4.3.4 Rotating to spatial correlator

As presented in Section 4.3.1, we can rotate the temporal correlator (4.26) to the spatial one using de Sitter invariance. From Eq. (4.9) we find as presented in [35],

$$G_f(0, \vec{x_1}, \vec{x_2}) = G_f\left(\frac{2}{H}\ln\left(|\vec{x_1} - \vec{x_2}|H\right)\right). \tag{4.28}$$

Here $G_f(0, \vec{x_1}, \vec{x_2})$ is the spatial correlator we want to find, while the right hand side of (4.28) is its corresponding temporal correlation function $G_f(t)$, whose spectral expansion is given by Eq. (4.26). Equation (4.28) is valid for distances much larger than the Hubble volume $|\vec{x_1} - \vec{x_2}| \gg \frac{1}{H}$ [35], which is the case in this Dissertation as we are interested in asymptotically large distances. From (4.28) we see that taking $t \to \frac{2}{H}\ln\left(|\vec{x_1} - \vec{x_2}|H\right)$ in the temporal correlator (4.26) we find the spatial correlator (using $\vec{x_1} - \vec{x_2} = \vec{x}$),

$$G_f(0, \vec{x_1}, \vec{x_2}) = \sum_{n=0}^{\infty} f_n^2 \frac{1}{(|\vec{x}|H)^{\frac{2\Lambda_n}{H}}}. \tag{4.29}$$

From (4.29) we observe that for asymptotically long distances we need to consider only the first non-zero terms in the expansion, since Λ_n increases with n. This makes the stochastic approach powerful. However, for the axion case it was found that the most significant contribution to the correlator can be given by either one of the first two excited levels of the expansion. This interesting dynamics that is further investigated in Section 6.6 arises due to the form of (4.29), where a larger f_n increases the contribution while a larger Λ_n diminishes it. In the next section, the stochastic method will be applied to the axion field.

5 Stochastic method for the axion

This section applies the calculations from Section 4 to the axion field (5.1), investigating the found eigenspectrum as a supersymmetric problem (5.2), and lastly studying the effect of the parameter α (5.3), which controls the eigenspectrum. The calculations and findings of this section form the basis for all the results presented in this Dissertation.

5.1 Eigenvalue equation

For the axion case, the one-point probability distribution from the Schrödinger-type equation (4.15) gives the PDF for the axion field values at the end of inflation (which we refer to as the misalignment angle, see Section 3.1). Using the potential (2.11) for our axion field $a(x)$, the operator $\tilde{D}_\phi$ in (4.16) becomes

$$\tilde{D}_a = \frac{1}{2}\frac{\partial^2}{\partial a^2} - \frac{1}{2}\left[\left(\frac{4\pi^2}{3H^4}\frac{V_0}{F_a}\sin\left(\frac{a}{F_a}\right)\right)^2 - \frac{4\pi^2}{3H^4}\frac{V_0}{F_a^2}\cos\left(\frac{a}{F_a}\right)\right], \tag{5.1}$$

since

$$\frac{\partial^2 V(a)}{\partial a^2} = \frac{\partial}{\partial a}\left(\frac{V_0}{F_a}\sin\left(\frac{a}{F_a}\right)\right) = \frac{V_0}{F_a^2}\cos\left(\frac{a}{F_a}\right). \tag{5.2}$$

Hence the eigenvalue equation (4.18) for $\psi_n(a)$ is

$$\frac{\partial^2\psi_n}{\partial a^2} - \left[\left(\frac{4\pi^2}{3H^4}\frac{V_0}{F_a}\sin\left(\frac{a}{F_a}\right)\right)^2 - \frac{4\pi^2}{3H^4}\frac{V_0}{F_a^2}\cos\left(\frac{a}{F_a}\right)\right]\psi_n = -\frac{8\pi^2\Lambda_n}{H^3}\psi_n. \tag{5.3}$$

In this context we define the dimensionless ratio α,

$$\alpha = \frac{V_0}{H^4}, \tag{5.4}$$

which will be a key quantity in the rest of this Dissertation, as it captures the dynamics between the axion potential V_0 and the Hubble parameter H. Implementing the misalignment angle ϕ from (2.6),

$$\frac{\partial}{\partial a} = \frac{1}{F_a}\frac{\partial}{\partial \phi}. \tag{5.5}$$

Then we can rewrite Eq. (5.3) in a simple form using (5.5) and (5.4),

$$\frac{\partial^2 \psi_n}{\partial \phi^2} - \left[\frac{16\pi^4}{9}\alpha^2 \sin^2\phi - \frac{4\pi^2}{3}\alpha\cos\phi\right]\psi_n = -\frac{8\pi^2 F_a^2 \Lambda_n}{H^3}\psi_n, \tag{5.6}$$

and we see that the eigenvalue $\Lambda_n \propto \frac{H^3}{F_a^2}$ on basis of dimensional analysis. For the sake of numerical computations, we rewrite the right hand side of equation (5.6) with the dimensionless β_n,

$$\frac{\partial^2 \psi_n}{\partial \phi^2} - \left[\frac{16\pi^4}{9}\alpha^2 \sin^2\phi - \frac{4\pi^2}{3}\alpha\cos\phi\right]\psi_n = -8\pi^2 \beta_n\, \psi_n, \tag{5.7}$$

where

$$\beta_n = \frac{F_a^2 \Lambda_n}{H^3}. \tag{5.8}$$

5.1.1 Solving with Mathematica

As $\phi(x)$ is essentially a dimensionless phase angle, the second term of (5.7), representing the Schrödinger potential of this eigenvalue equation, is clearly periodic over 2π. Therefore, periodic boundary conditions over $[-\pi, \pi]$ were implemented for the eigenfunctions. Eq. (5.7) was solved numerically in Mathematica using the NDEigensystem function with a discretisation finite element method, giving both the eigenfunctions and eigenvalues. NDEigensystem normalises the eigenfunctions automatically to unity. In addition, all the eigenfunctions were assumed to be real.

5.1.2 Eigenspectrum for $\alpha = 1$

We concentrate first on the case $\alpha = 1$, corresponding to $V_0 = H^4$ (see Eq. (5.4)), which is expected to give us a typical eigenspectrum. The first seven eigenvalues for $\alpha = 1$ are tabled below, represented using the dimensionless β_n (5.8) introduced above.

n	β_n
0	0
1	0.32680
2	0.32680
3	0.64011
4	0.64011
5	0.93889
6	0.93889

Table 1: The first seven eigenvalues for the eigenvalue equation (5.7) where β_n is found by dividing the value from NDEigensystem by $-8\pi^2$.

A key observation is that the eigenvalues come in pairs, except for $\beta_0 = 0$. This was assumed to be an exact result in the light of the numerical accuracy of NDEigensystem, after the eigenvalues from both the $[-\pi, \pi]$ and a comparison range $[0, 2\pi]$ were found to differ from their degenerate partners only up to the $\sim$ 7th decimal. This degeneracy is a consequence of our eigenvalue equation (5.7) having the form of a supersymmetric QM equation, which is further investigated in Section 5.2. The first five eigenfunctions are represented in Figure 3. From the eigenvalues in Table 1 we see that ψ_1 and ψ_2 are degenerate, and likewise for ψ_3 and ψ_4. The symmetry of these eigenfunctions is expected from the symmetry of our axion potential. As these eigenfunctions enter the spectral coefficients (4.27), studying their behaviour is essential in understanding their contribution to the axion density correlator (see Section 5.3.2).

To investigate these eigenfunctions further, we note that the minimum of the axion potential (2.11) is at $\phi = 0$ while its first maxima lie at $\phi = \pm\pi$. Hence, from Fig. 3 we see that the ground state ψ_0 is centred at the minimum of the potential, as would be expected since it gives directly the equilibrium probability distribution (4.19), where the most likely location of the axion is at rest at the bottom of the potential. However, for the higher order eigenfunctions we notice that at each degeneracy level one function is centred at $\phi = 0$, and the other one at the maxima $\phi = \pm\pi$.

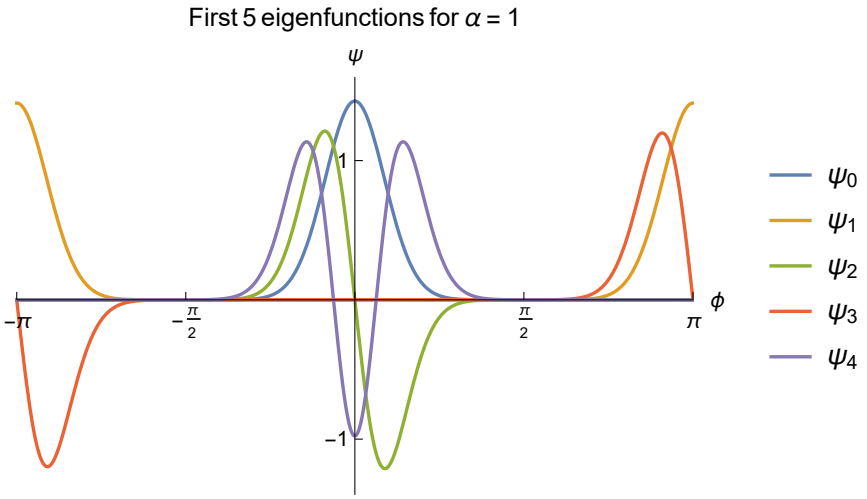

Figure 3: The first five eigenfunctions of the eigenvalue equation (5.7) for $\alpha = 1$, with the ground state ψ_0 centred at $\phi = 0$.

In addition, one is always even and one is odd w.r.t $\phi = 0$. As our chosen density function $f_{\text{full}}(\phi)$ (3.3) is even w.r.t $\phi = 0$, if ψ_n is odd, the spectral coefficient (4.27) will systematically be zero. Hence, at each eigenlevel only one of the eigenfunctions brings a contribution to the spectral expansion of the axion density correlator. A final point to note about the degenerate eigenfunctions is that the one centred on the maximum $\phi = \pm\pi$ has always one node less over one period than its partner centred at $\phi = 0$. By node we mean a point where the function crosses the x-axis. For example, from Figure 3 it is clear that ψ_4, centred on the minimum, has two nodes while its counterpart, ψ_3, has only one node (at $\pm\pi$). This behaviour is also explained through supersymmetry in the next section.

Overall, finding non-perturbative states at each eigenlevel is significant because of the common linear approximation used in the axion context. In the rest of the Dissertation, we use the word "perturbative" to describe states centred around the minimum of the potential, which can be approached with a perturbative treatment (e.g. quadratic approximation). On the other hand, non-perturbative states are not centred at the minimum, and are missed by the perturbative treatment. The dynamics between perturbative and non-perturbative states is ultimately defining the dominant contribution to the spectral expansion of the axion correlator.

5.2 Supersymmetric spectrum

5.2.1 Supersymmetric quantum mechanics

We study our eigenvalue equation (5.7) in the context of quantum mechanics, as a supersymmetric Schrödinger equation, to understand why it gives a degenerate spectrum. The basic idea behind supersymmetry (SUSY) arising from a one-dimensional Schrödinger-type equation is that for the original Hamiltonian of the theory, a partner Hamiltonian can be defined, possessing the same energy spectrum as the original one (but usually without the ground state) [42]. This enables to find a partner potential as well as "bosonic" and "fermionic" operators that allow to move between the original states and their SUSY partners. In this Dissertation, we will use the mathematical framework of SUSY to understand the spectrum of our eigenvalue equation, without deepening the analysis into the breaking of supersymmetry. For further information on the SUSY dynamics, the reader is referred to [43, 44] and for the particular case of the PQ symmetry, to [45].

Supersymmetry can be useful in problems with both perturbative and non-perturbative states. If the originally non-perturbative states become perturbative for the SUSY treatment, they can be computed using the partner Hamiltonian (one important application is the AdS-CFT correspondence). This is also of interest for our axion case due to the common linear approximation, which captures only the perturbative states.

5.2.2 Mathematical structure

Our starting point is the eigenvalue equation (5.7). As this is derived from a Fokker-Planck equation as introduced in Section 4.3.2, we follow the approach of Bernstein and Brown in [46]. We can rewrite this Schrödinger-type equation using a Hamiltonian,

$$H\psi_n = \lambda_n \psi_n, \quad H = A^\dagger A, \tag{5.9}$$

where ψ_n are the eigenstates of the spectrum, and we identify,

$$\lambda_n = 8\pi^2 \beta_n. \tag{5.10}$$

Here we note that λ_n refers to the eigenvalues of this Hamiltonian formalism, while Λ_n are the eigenvalues stemming from the stochastic spectral expansion (4.26). Next we define the operators,

$$A = \frac{4\pi^2}{3}\alpha \sin\phi + \frac{\partial}{\partial\phi}, \tag{5.11}$$

$$A^\dagger = \frac{4\pi^2}{3}\alpha \sin\phi - \frac{\partial}{\partial\phi}, \tag{5.12}$$

to find

$$A^\dagger A = \left(\frac{4\pi^2\alpha}{3}\right)^2 \sin^2\phi - \frac{4\pi^2\alpha}{3}\cos\phi - \frac{\partial^2}{\partial\phi^2}. \tag{5.13}$$

Combining this with (5.9) and (5.10), we see that (5.13) indeed gives the original eigenvalue equation (5.7). Having thus set up our eigenvalue equation in a quantum mechanical context, we can use supersymmetry to explore its properties. We define the nilpotent operators Q and $Q^\dagger$,

$$Q = \begin{pmatrix} 0 & 0 \\ A & 0 \end{pmatrix}, \qquad Q^\dagger = \begin{pmatrix} 0 & A^\dagger \\ 0 & 0 \end{pmatrix}. \tag{5.14}$$

Using these, a supersymmetric matrix Hamiltonian can be written (see [46]),

$$H_{\text{SUSY}} = Q^\dagger Q + Q Q^\dagger = \begin{pmatrix} H_+ & 0 \\ 0 & H_- \end{pmatrix}, \tag{5.15}$$

where $H_+ = A^\dagger A$, the original Hamiltonian, while $H_- = AA^\dagger$, its SUSY partner. Q and $Q^\dagger$ are called supercharges, and together with $H_{\rm SUSY}$ they form the closed superalgebra $sl(1/1)$, characterised by the vanishing commutator of $H_{\rm SUSY}$ with both Q and $Q^\dagger$ [42]. From the partner Hamiltonians we can directly deduce the SUSY partner potentials. Denoting $U(\phi)$ as the QM potential in the eigenvalue equation (5.7), and its supersymmetric partner as $B(\phi)$, we find,

$$U(\phi) = \left(\frac{4\pi^2\alpha}{3}\right)^2 \sin^2\phi - \frac{4\pi^2\alpha}{3}\cos\phi, \tag{5.16}$$

$$B(\phi) = \left(\frac{4\pi^2\alpha}{3}\right)^2 \sin^2\phi + \frac{4\pi^2\alpha}{3}\cos\phi. \tag{5.17}$$

In quantum mechanical SUSY literature it is also common to talk about a "superpotential", which in our case would be

$$W(\phi) = \frac{4\pi^2\alpha}{3}\sin\phi. \tag{5.18}$$

The original potential is recovered through the well-known Riccati equation [42],

$$U(\phi) = W^2(\phi) - W'(\phi). \tag{5.19}$$

To avoid confusion, we also note that it is common practice in cosmology to label the original potential, $U(\phi)$ in the context of this Dissertation, as $W(\phi)$, so the reader should make note of our conventions (5.16) and (5.18). The partner potentials are represented in Figure 4, from which a translation symmetry between them is clear,

$$U(\phi + \pi) = B(\phi). \tag{5.20}$$

Hence, the SUSY partner potential for our eigenvalue equation (5.7) is just a translation by π.

This is ultimately the reason behind our degenerate spectrum, and why we call the eigenvalue equation (5.7) "supersymmetric". We can think of our original potential $U(\phi)$ including its superpartner in itself, and hence both the states of the original potential and its superpartner $B(\phi)$ are visible in the eigenspectrum, differing by translations of π. This can be seen as self-duality, and ultimately originates from the shift symmetry of the axionic potential (2.11) from QCD theory,

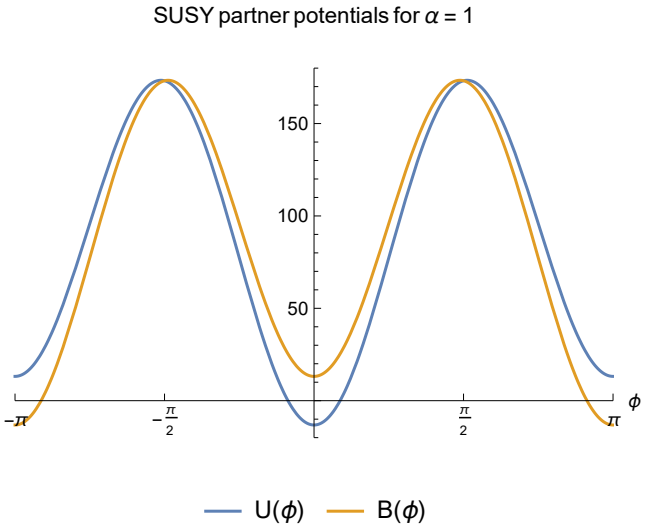

Figure 4: The potential $U(\phi)$ in the original eigenvalue equation and its supersymmetric partner $B(\phi)$.

$$-V_0 \cos\phi = V_0 \cos(\phi + \pi). \tag{5.21}$$

Here we emphasise that the Schrödinger potential $U(\phi)$ in the eigenvalue equation (5.7) is derived from the axion potential (2.11). Hence, without the shift symmetry (5.21), there would be no degeneracy in the eigenspectrum. This is explored further in Section 5.2.4 where we break the translation symmetry by introducing a small deviation to the axion potential. However, next we will explore the degenerate spectrum of Eq. (5.7) with the mathematical tools introduced above.

5.2.3 Exploring the degeneracy

Following [46], the eigenstate ψ can be expanded into a column vector with 2 components,

$$\Psi = \begin{pmatrix} \psi_+ \\ \psi_- \end{pmatrix}. \tag{5.22}$$

The upper part of H_{SUSY} (5.15), H_+, acts on the upper part of Ψ and therefore gives the original

eigenfunctions ψ_n. However, $Q\psi_n$ will also be an eigenfunction of H_{SUSY} with the same eigenvalue as ψ_n, because of the vanishing commutator of Q and H_{SUSY} [46]. Hence we get two stacks of states with degenerate eigenvalues, corresponding to the "bosonic" ψ_+ and the "fermionic" ψ_- [46]. We can switch between these partner states as

$$Q\psi_{n+} = \psi_{n-} \,, \tag{5.23}$$

$$Q^\dagger\psi_{n-} = \psi_{n+} \,. \tag{5.24}$$

Indeed, one interpretation for the action of the supercharges Q and $Q^\dagger$ defined in (5.14) is to move between fermionic and bosonic degrees of freedom [42]. The only exception is the ground state which conventionally does not have a SUSY partner. This is seen in our axion spectrum by the fact that there is only one state with the lowest eigenvalue $\Lambda_0 = 0$. It is also worth noting that the SUSY partner states in (5.23) and (5.24) are not normalised. To investigate this behaviour, we start by studying the spectrum of our partner potential $B(\phi)$. The eigenvalues are found to be the same as for the original potential, as expected. From the eigenspectrum of $B(\phi)$ in Figure 5 we note that the same symmetry pattern as for the original spectrum in Figure 3 emerges: one

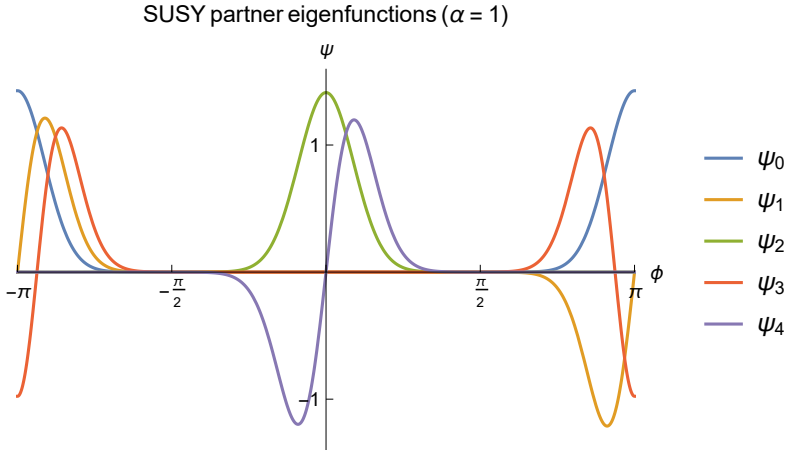

Figure 5: The spectrum of the SUSY partner potential $B(\phi)$.

of the degenerate eigenfunctions is odd and the other one even with respect to $\phi = 0$. We also observe the increase of nodes from one eigenfunction to its partner, and we see that the ground state ψ_0 has shifted to be now centred at the minimum of the partner potential $B(\phi)$ at $\pm\pi$, which is demonstrated in Figure 6. This is an example of the perturbative and non-perturbative states switching position – the states around $\pm\pi$ that were non-perturbative for the original potential become perturbative for the SUSY partner potential, introducing the possibility to study the degenerate SUSY partner states instead of the originally non-perturbative ones. In this context we note that even though conventional supersymmetric theory does not give a ground state for the partner Hamiltonian, as it would generally not be normalisable [42], we have a finite integration range due to the periodicity of the potential, and can thus normalise any non-divergent function over the period. This explains the ground state in our SUSY spectrum.

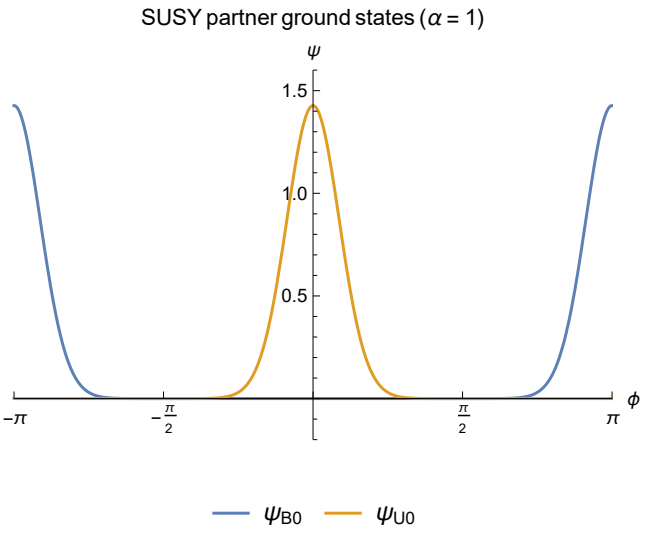

Figure 6: The ground states of the partner potentials U and B. The translation symmetry by π is apparent.

Figure 7 allows a direct comparison between the first two eigenlevels of the partner potentials. It is important to note that due to the translation symmetry, both U and B have two degenerate states at each eigenlevel, and in addition we would expect the corresponding U and B states to be the same but with a shift of π. This is clearly observed with both eigenlevels, where for example ψ_{U4} is ψ_{B4} translated by π along the x-axis. The ψ_1 case is interesting, because ψ_{B1} is actually the ground state of $U(\phi)$, whereas ψ_{U1} is the ground state of $B(\phi)$. This implies that for our periodic potential, the SUSY partner of the non-degenerate ground state is at the same time the first excited state of the spectrum. We also note that the eigenfunctions are unique up to a sign, and therefore the sign given by Mathematica is arbitrary (see e.g. ψ_{B2} and ψ_{U2}).

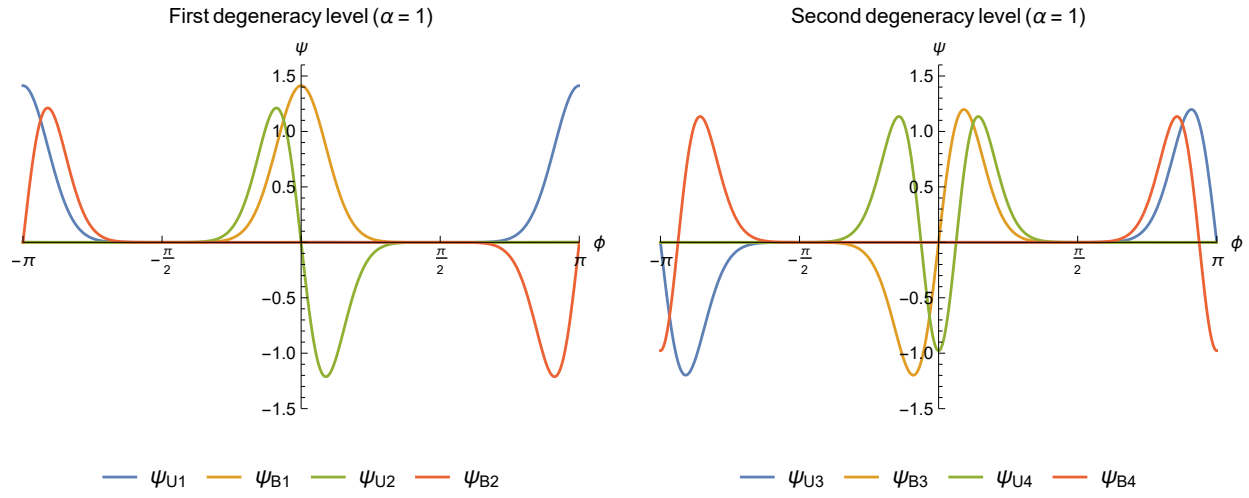

(a) Eigenfunctions with $\lambda_1 = \lambda_2$.

(b) Eigenfunctions with $\lambda_3 = \lambda_4$.

Figure 7: The degenerate states of the SUSY partner potentials for the first two energy levels. The potential to which the state belongs is labelled as a subscript for ψ_n.

A second trend is that ψ_{n+1} has one node more than ψ_n. This can be seen for example in Figure 7a, where ψ_{U1} has no nodes, but its degenerate counterpart ψ_{U2} has one. Similarly in Figure 7b, ψ_{U3} has one node but ψ_{U4} has two. To link this to SUSY theory, we note that as explicitly shown in [42], acting with the operator A ($A^\dagger$) (see Eqs. (5.11), (5.12)) onto a state ψ_+ (ψ_-) returns an eigenfunction of H_- (H_+) but in addition, this operation removes (adds) a node from the eigenfunction. The results of applying the operators A and $A^\dagger$ numerically to the eigenstates in the second eigenlevel are shown in Figure 8.

As mentioned previously, the states obtained with A or $A^\dagger$ are not normalised (see Eqs. (5.23) and (5.24)). Focusing first on Figure 8a, we see that by applying A on ψ_{U4} (green) we find the (non-normalised) state ψ_{B3} (yellow). Similarly, acting $A^\dagger$ on the partner state ψ_{B3} (red), we recover ψ_{U4} (blue), again with a larger scale than the normalised states. One can see explicitly that these SUSY partner states are the same as the original ones by checking that their nodes coincide. The same pattern is observed in Figure 8b, where again the states emerging under the action of the operators are not normalised. In conclusion, by explicit calculation on Mathematica we have shown the supersymmetric theory introduced in Section 5.2.2 to hold for our axion eigenvalue

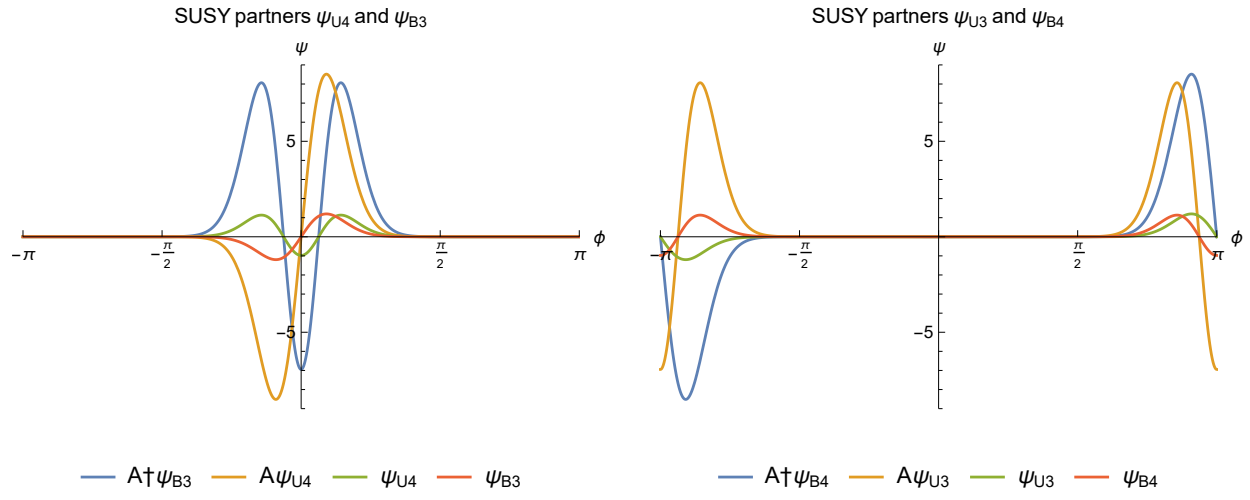

(a) (b)

Figure 8: Switching between SUSY partner states using the A and $A^\dagger$ operators.

equation (5.7). It is worth noting that while these results were evaluated for $\alpha = 1$, they apply to other α values as well, and therefore contribute to understanding the behaviour of the spectral coefficients (4.27). Especially the parity and the perturbativeness of the eigenfunctions is key in evaluating the spectral expansion of the axion correlator.

5.2.4 Breaking the translation symmetry

Finally, we study the case where we explicitly break the shift symmetry of the original axion potential (see Eq. (5.21)) to get non-degenerate eigenvalues. This is important, because the physical axion potential is most probably not a pure cosine, as assumed in this Dissertation, but has correction terms breaking the original symmetry. We introduce a small deviation of $\cos^2\phi$ to the original potential,

$$V(\phi) = -V_0 \cos\phi - \epsilon V_0 \cos^2\phi, \tag{5.25}$$

where the parameter ϵ controls how much this potential deviates from the original one. Then finding the derivatives (which must be taken w.r.t. the axion field $a(x)$),

$$\frac{\partial^2 V}{\partial a^2} = \frac{\partial}{\partial a}\left[\frac{V_0}{F_a}\sin\left(\frac{a}{F_a}\right) + \epsilon\frac{V_0}{F_a}\sin\left(2\frac{a}{F_a}\right)\right] = \frac{V_0}{F_a^2}\left[\cos\left(\frac{a}{F_a}\right) + 2\epsilon\cos\left(2\frac{a}{F_a}\right)\right], \tag{5.26}$$

and again using our definition of ϕ (2.6), and α (5.4), the eigenvalue equation (4.18) becomes

$$\frac{\partial^2\psi_n}{\partial\phi^2} - \frac{16\pi^4}{9}\alpha^2\big(\sin\phi + \epsilon\sin 2\phi\big)^2\psi_n + \frac{4\pi^2}{3}\alpha\big(\cos\phi + 2\epsilon\cos 2\phi\big)\psi_n = -\frac{8\pi^2 F_a^2\Lambda_n}{H^3}\psi_n. \tag{5.27}$$

From Eq. (5.27) we can immediately recognise the new Schrödinger potential $U(\phi)$,

$$U(\phi) = \frac{16\pi^4}{9}\alpha^2\big(\sin\phi + \epsilon\sin 2\phi\big)^2 - \frac{4\pi^2}{3}\alpha\big(\cos\phi + 2\epsilon\cos 2\phi\big). \tag{5.28}$$

We now find the superpotential using the Riccati equation (5.19),

$$W(\phi) = \frac{4\pi^2}{3}\alpha\big(\sin\phi + \epsilon\sin 2\phi\big), \tag{5.29}$$

and the partner potential is easily found from this superpotential,

$$B(\phi) = \frac{16\pi^4}{9}\alpha^2\big(\sin\phi + \epsilon\sin 2\phi\big)^2 + \frac{4\pi^2}{3}\alpha\big(\cos\phi + 2\epsilon\cos 2\phi\big). \tag{5.30}$$

Figure 9 demonstrates how the correction term affects the shape of $U(\phi)$ and its supersymmetric partner. To show the deviation clearly we used $\epsilon = 1$. Just as for the original potential, the minimum of both $V(\phi)$ (the axionic potential) and $U(\phi)$ is at $\phi = 0$, but on the other hand $B(\phi)$ has now its minima in the middle of the period, from which we expect the symmetry of the eigenfunctions to partly break. As we are interested in the case of small correction terms to the axion potential, we use $\epsilon = 0.2$ for the following calculations.

Implementing the eigenvalue equation (5.27) in Mathematica as for the previous calculations, we find the first five eigenvalues. These are the same, as expected, for the eigenvalue equation of the new $B(\phi)$ potential, since the supersymmetric partner potentials have the same eigenlevels. These are listed in Table 2, from which we first note that the degeneracy has been lifted, as our new potential (5.25) does not have a shift symmetry by π.

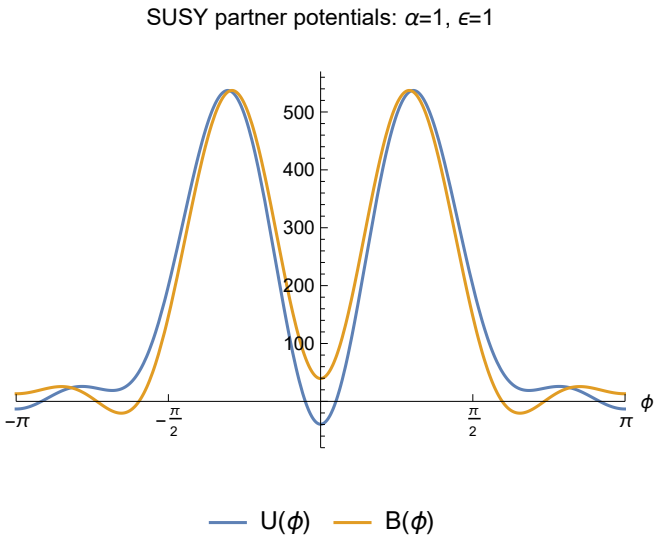

Figure 9: The changed potential $U(\phi)$ and its supersymmetric partner $B(\phi)$.

n	β_n
0	0
1	0.20526
2	0.41932
3	0.45450
4	0.63918

Table 2: The first five eigenvalues (see β_n (5.8)) for the eigenvalue equation (5.27).

Hence, the supersymmetry is not apparent in the spectrum anymore. The corresponding eigenfunctions for both the U and B potentials are shown in Fig. 10. Comparing the U states in Fig. 10a with the unbroken spectra in Fig. 3, as well as the B spectrum in 10b with Fig. 5, we observe that the new eigenfunctions are still highly symmetric. However, the symmetry breaking manifests itself through the location of the excited eigenfunctions, which are now centred differently than in the original spectra. We can again define the A and $A^\dagger$ operators,

$$A = \frac{4\pi^2}{3}\alpha\big(\sin\phi + \epsilon\sin 2\phi\big) + \frac{\partial}{\partial\phi}, \quad A^\dagger = \frac{4\pi^2}{3}\alpha\big(\sin\phi + \epsilon\sin 2\phi\big) - \frac{\partial}{\partial\phi}. \tag{5.31}$$

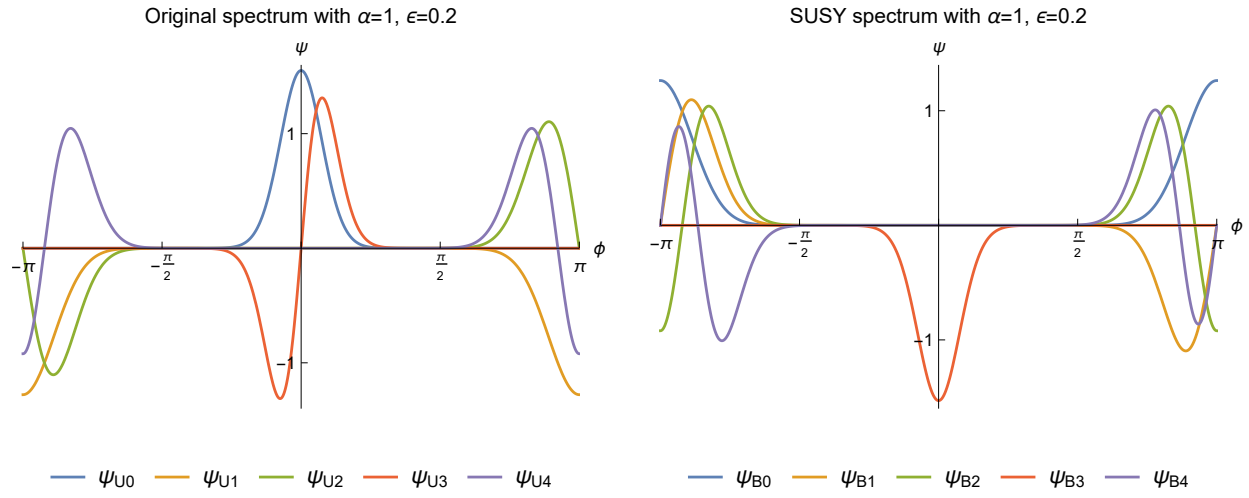

(a) Eigenfunctions for U potential.

(b) Eigenfunctions for B potential.

Figure 10: The eigenstates of the modified potential and its SUSY partner.

Starting from a U state, we use A to obtain the (non-normalised) B state with the same eigenvalue, and vice versa with $A^\dagger$. This is demonstrated in Figure 11 for the fourth excited level, where e.g. acting $A^\dagger$ on ψ_{B4} (red) gives us back the (non-normalised) U state ψ_{U4} (blue). Hence, as predicted, we can move between the U and B spectra using the operators (5.31). In conclusion, by breaking the shift symmetry in the original axion potential, we find a classical supersymmetric spectrum, where the degeneracy is hidden in the SUSY partner states. This has important implications for the study of axion potentials that have correction terms to the conventional cosine potential. Having thus investigated the axion eigenspectrum for a fixed $\alpha = 1$, we turn next to study the effect of α.

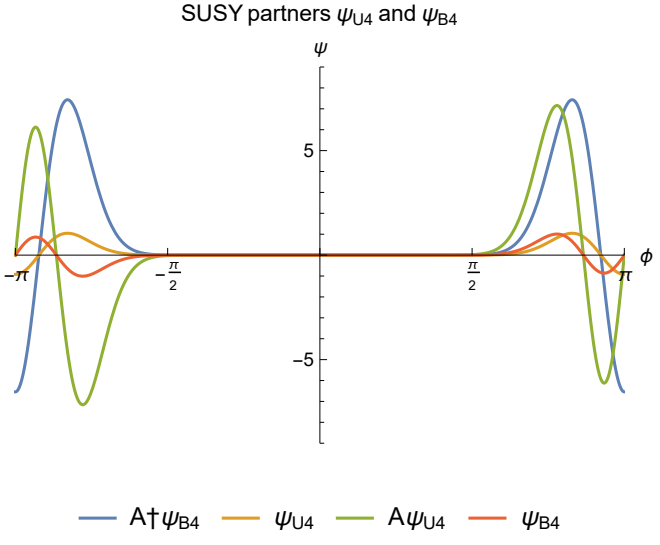

Figure 11: Switching between the SUSY partner states of the U and B spectra using the operators A and $A^\dagger$.

5.3 Impact of the α parameter

5.3.1 Free-field limits

In Section 5.1 it was shown that the eigenspectrum of the axionic eigenvalue equation depends on the dimensionless ratio $\alpha = \frac{V_0}{H^4}$ (5.4), which is a key quantity for our axion theory. This is because V_0 gives the amplitude of the axion potential, whereas H^4 is directly linked to the axion energy density. Hence, α controls the dynamics of the equilibrium probability distribution (4.13) given by the stochastic method, which sets the misalignment angle (see Section 3.1). To understand the axion field behaviour in the limit of small and large α, we list the first seven eigenvalues from $\alpha = 0$ to 3 in Table 3.

α	0	0.5	1	3
λ_0	0	0	0	0
$\lambda_{1,2}$	1.00	12.6	25.8	78.5
$\lambda_{3,4}$	4.00	24.1	50.5	156
$\lambda_{5,6}$	9.00	34.1	74.1	232

Table 3: The first seven eigenvalues for different α, where λ_n is the full Schrödinger-type equation eigenvalue as defined in (5.10) in SUSY context.

We first note that for $\alpha = 0$, Eq. (5.7) becomes a classical QM particle-in-a-box -type scenario, from which we expect the eigenvalues to be proportional to n^2. This is indeed observed in Table 3 for the first four levels. We note that $\lambda_{1,2}$ corresponds to $n = 1$, $\lambda_{3,4}$ to $n = 2$, exc. However, as our boundary conditions do not restrict the eigenfunctions to vanish at the edges of the period, we also have the ground state with $\lambda_0 = 0$. Low values of α thus correspond to plane waves, which essentially do not feel the potential. Mathematically this happens because α is the factor controlling the potential term in the eigenvalue equation (5.7). Physically, this free-field behaviour corresponds to $H^4 \gg V_0$, where the energy of the axion is enough for climbing the potential, leading to an almost equal probability for any value of the misalignment angle. For completeness, we note that as will be found in Section 6, this free-field behaviour cannot be approximated by the perturbative treatment, unlike the other α limit.

For large α, the axion energy density is much lower than the amplitude of the potential ($H^4 \ll V_0$). The axion is essentially oscillating as a massive particle at the bottom of the potential, which can therefore be approximated as quadratic. This is the classical case of a harmonic oscillator, with the eigenvalues increasing approximately linearly for $\alpha = 1$ and $\alpha = 3$, as observed in Table 3. This quadratic free-field behaviour translates into a high probability for a low misalignment angle, and corresponds to the case where the linear approximation most commonly used in axion literature is valid (see e.g. [47] for a detailed discussion on this approximation in the context of the axion isocurvature power spectrum).

Figure 12 demonstrates the energy scales of the two free-field limits discussed above, where we can think of H^4 as quantising the axion energy and hence corresponding to the green ($H^4 \ll V_0$) and yellow ($H^4 \gg V_0$) lines. The axion potential is shown in blue. One of our main goals in the study of the axion correlator through the stochastic approach is to investigate the region in the α parameter space where neither of these free-field limits is valid. As most of the current work on axions has been done using the linear approximation, the dynamics of an axion in this middle region is yet unexplored. The results on this are presented in Section 6.

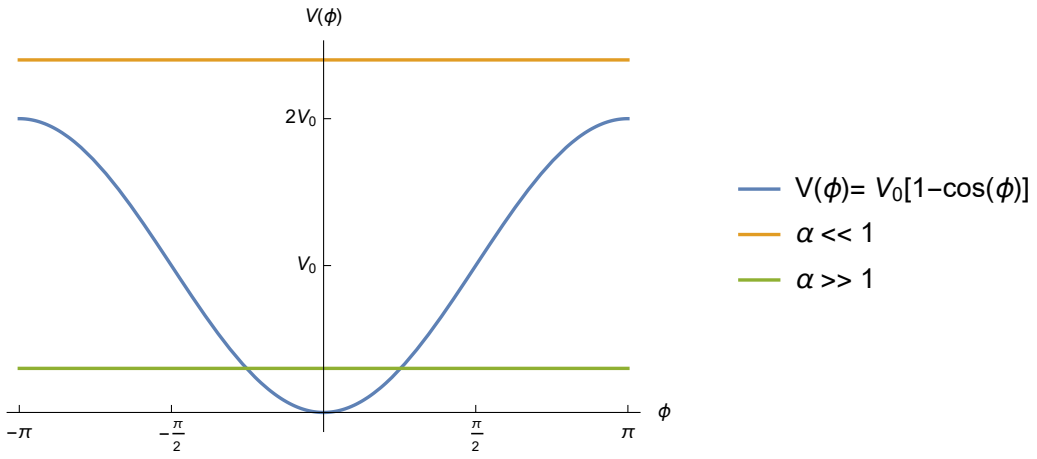

Figure 12: The axion potential $V(\phi)$ with the free-field limits of α.

5.3.2 Behaviour of the spectral coefficients

The ground state of the spectral expansion (4.26) gives directly the probability distribution for the misalignment angle (4.19), and hence the probability for the axion to be found in different regions along its potential can be read from the shape of the ground state. From Figure 13 we observe that the ground state is spreading out with decreasing α. For low α, the energy density starts to dominate over the potential, giving the axion freedom to move along the potential. This then translates into the ground state becoming more uniform across the misalignment angle range, mirroring the probability density which becomes flat in the limit $\alpha \to 0$. On the other hand, in the large α limit, the axion is confined near the minimum of the potential, which is reflected in a sharp Gaussian-like ground state centred at $\phi = 0$.

The overlap of the ground state ψ_0 with the excited state ψ_n defines the spectral coefficients f_n (4.27). The perturbative states centred around the minimum will have naturally a higher spectral coefficient (provided that they have the correct parity), while the contribution from non-perturbative states will depend strongly on the value of α. This can be thought of as a tunnelling problem. When the overlap is small, the tunnelling probability to go from the ground state to a higher state centred on a different symmetry point away from the minimum is low. This is illustrated in Figure 14a for $\alpha = 0.5$, where the overlap is practically zero. With a larger overlap (see Fig. 14b), the tunnelling of our axion particle is more probable, which is reflected in a higher value of f_n. This non-perturbative first excited state ψ_1 in Fig. 14b gives the dominating contribution to the isocurvature power spectrum for low α (see Section 6).

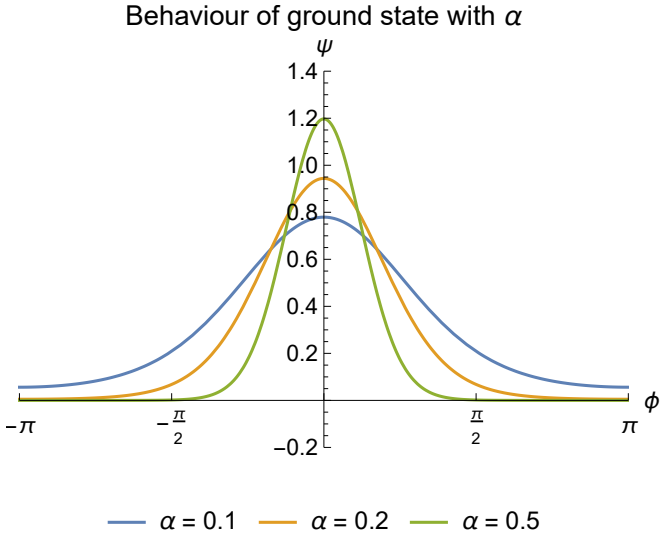

Figure 13: The ground state ψ_0 spreads out with decreasing α.

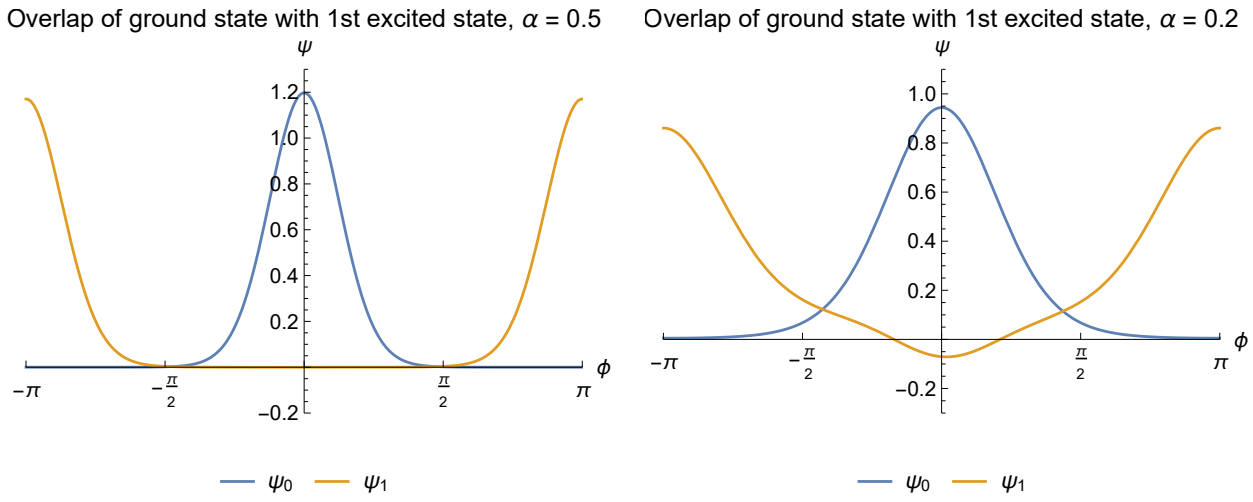

(a) Overlap for $\alpha = 0.5$

(b) Overlap for $\alpha = 0.2$

Figure 14: Visualising the overlap between the ground state and the first excited state for $\alpha = 0.5$ and $\alpha = 0.2$. Numerical errors due to a small α value are observed in the shape of ψ_1 in Fig. 14b.

To explore this dependence of f_n on α, we start with the simplest correlator – the temporal correlator of the field itself. This is defined as the expectation value of the complex $U(1)_{PQ}$ field $\chi(x)$,

$$\langle \chi(0)\chi^*(t)\rangle = F_a^2 \langle e^{i\phi(0)} e^{-i\phi(t)}\rangle, \tag{5.32}$$

where we suppose that the radial part of the field $\rho(x)$ is at its vev F_a. From (5.32) we see that the function f needed for the stochastic approach is $e^{i\phi}$, and hence the parity of the eigenfunctions is not relevant. From Eqs. (4.26) and (4.27) we find,

$$\langle e^{i\phi(0)} e^{-i\phi(t)}\rangle = \sum_n \langle 0|e^{i\phi(x)}|n\rangle e^{-\Lambda_n t} \langle n|e^{-i\phi(x)}|0\rangle, \tag{5.33}$$

$$f_n = \int_{-\pi}^{\pi} e^{i\phi} \psi_0(\phi)\psi_n(\phi) d\phi \,. \tag{5.34}$$

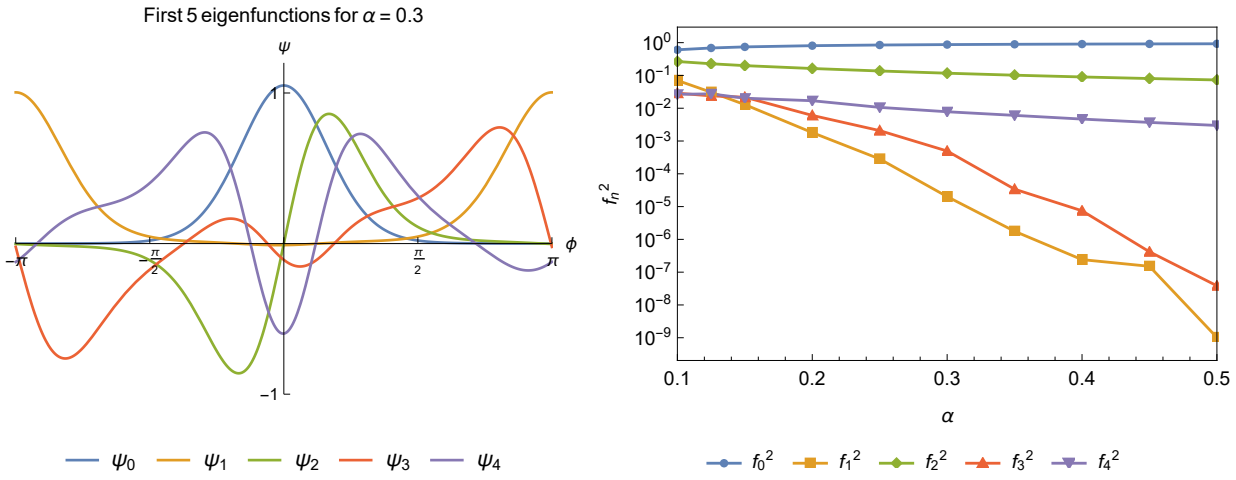

(a) The eigenspectrum for $\alpha = 0.3$.

(b) The spectral coefficients as a function of α.

Figure 15: The non-perturbative states ψ_1 and ψ_3 have a smaller overlap with the ground state than their corresponding degenerate partners ψ_2 and ψ_4.

The overlap between the ground and excited states of $\alpha = 0.3$ can be visualised from Figure 15a. Fig. 15b shows the corresponding spectral coefficients. We observe, as expected, that f_1 and f_3 of the non-perturbative states are smaller for all α than f_2 and f_4, correspondingly, the states centred at $\phi = 0$. We also note that the spectral coefficients increase systematically with decreasing α for all n, except for $n = 0$, where there is no excited state involved. This is due to the spreading of the eigenstates with decreasing α, as was illustrated in Fig. 13 for the ground state, introducing a higher overlap. From Fig. 15b we conclude that for the correlator of $f = e^{i\phi}$, the contribution from the non-perturbative states effectively vanishes for increasing α. This will also be true for our actual density correlator, and is significant for the linear approximation.

Figure 15 also demonstrates how numerical errors for small α values become visible in the higher excited states. For example, ψ_3 in Fig. 15a should be ψ_2 shifted by π, instead it seems like a complicated linear superposition. This could be due to the eigenvalues of different levels getting closer together for decreasing α, making it harder to differentiate the eigenfunctions numerically. The same behaviour is seen in Fig. 14b, where ψ_1 should have the same shape as the corresponding function in Fig. 14a. The numerical errors will be further discussed in Section 7.3. Using all these findings about the stochastic axion, we move on to evaluate its power spectrum.

6 Results

This section presents the results from the stochastic axion model developed in this Dissertation. The mathematical results include the isocurvature power spectrum (6.1) and the axion dark matter parameter (6.2). The approximation schemes used to analyse the results are detailed in Section 6.3. Finally, the cosmological parameter values found are presented in Section 6.4 (the axion decay constant) and in Section 6.5 (the Hubble parameter). The novel feature revealed by the stochastic approach, the transition region, is carefully analysed in Section 6.6.

6.1 Isocurvature power spectrum

Our goal is to compare the axion isocurvature contribution predicted by our theory to the current experimental bound derived from the Planck satellite data (see Section 3.4). The physical quantity capturing these isocurvature fluctuations is the axion density correlator, which measures how the current axion energy density is correlated between asymptotically distant locations (see Section 1.3). Both the adiabatic and isocurvature contributions are conventionally given in terms of their power spectrum, which in cosmology is generally defined as the Fourier transform of a spatial two-point correlation function [12]. Hence, we need to relate the physical axion energy density correlator to the power spectrum of the isocurvature component it produces. For the calculations, we recall that the axion energy density correlator has the form (4.29) from the stochastic method, and it involves the eigenfunctions and eigenvalues from the axion eigenvalue equation (5.7), which were investigated in detail in Section 5. More importantly, the function $f(\phi)$ entering the spatial correlator through the spectral coefficients (4.27) is the axion energy density function $f_{\text{full}}(\phi)$ (3.3), discussed in Section 3.3.

In the following we use the approach presented in [41]. The isocurvature between CDM and radiation (γ) is defined as

$$S \equiv \frac{\delta\rho_a}{\rho_a} - \frac{3}{4}\frac{\delta\rho_\gamma}{\rho_\gamma}. \tag{6.1}$$

Then, choosing a gauge where the "normal" curvature fluctuations will be apparent in the scale factor, and assuming that only fluctuations of the axion field at the end of inflation are contributing to the dark matter isocurvature component [41], we can write

$$S = \frac{f(a(x)) - \langle f(a)\rangle}{\langle f(a)\rangle}, \tag{6.2}$$

where $f(a)$ is our axion energy density function f_{full}. Here we note that we use $a(x)$ to emphasise that these calculations apply to the actual axion field, but for computation purposes the dimensionless $\phi(x)$ will be used (for the correct dimensional relation see Eq. (2.6)). In (6.2), we need to subtract the average axion density $\langle f(a)\rangle$ to get fluctuations. From this we find the isocurvature equal-time correlator [41],

$$\langle S(0)S(\vec{x})\rangle = \frac{\langle f(a(0))f(a(\vec{x}))\rangle - \langle f(a)\rangle^2}{\langle f(a)\rangle^2}, \tag{6.3}$$

where we identify the spatial axion energy density correlator in the numerator. Using its spectral expansion (4.29), we see that the first expansion term ($\Lambda_0 = 0$) cancels the second term in the isocurvature correlator (6.3) since

$$\langle f(a(0))f(a(\vec{x}))\rangle = \langle f\rangle^2 + \sum_{n=1}^{\infty} f_n^2 \frac{1}{(|\vec{x}|H)^{\frac{2\Lambda_n}{H}}}, \tag{6.4}$$

where $f_0 = \langle 0|f|0\rangle = \langle f\rangle$ gives the expectation value of $f(a)$. Using (6.4), the final form of the isocurvature correlator (6.3) for our density function $f(a)$ (3.3) is

$$\langle S(0)S(\vec{x})\rangle = \sum_{n=1}^{\infty} \frac{f_n^2}{\langle f\rangle^2} \frac{1}{(|\vec{x}|H)^{\frac{2\Lambda_n}{H}}}. \tag{6.5}$$

For the asymptotic limit, we take only the leading non-zero term $n = d$,

$$\langle S(0)S(\vec{x})\rangle \approx \frac{f_d^2}{\langle f\rangle^2}(|\vec{x}|H)^{\frac{-2\Lambda_d}{H}}. \tag{6.6}$$

The isocurvature power spectrum is defined as the Fourier transform of this correlator,

$$P(k) = \frac{k^3}{2\pi}\int d^3x e^{i\vec{k}\vec{x}}\langle S(0)S(\vec{x})\rangle. \tag{6.7}$$

Hence using (6.6) to evaluate (6.7) [41],

$$P(k) \approx \frac{2}{\pi}\frac{f_d^2}{\langle f\rangle^2}\Gamma\left(2-\frac{2\Lambda_d}{H}\right)\sin\left(\frac{\Lambda_d\pi}{H}\right)\left(\frac{k}{\tilde{k}}\right)^{\frac{2\Lambda_d}{H}}, \tag{6.8}$$

where $\tilde{k}$ is defined as the horizon scale at the end of inflation. To make our comparison with the curvature power spectrum (the adiabatic component), measured at the pivot scale $k_P = 0.05$ Mpc^{-1}, we use the e-fold number N_P [41],

$$N_P \equiv \ln\left(\frac{\tilde{k}}{k_P}\right) \approx 56 + \frac{1}{2}\ln\left(\frac{H_I}{8\times 10^{13}\text{ GeV}}\right), \tag{6.9}$$

where H_I is the inflationary Hubble parameter. Then approximating $\sin(\frac{\Lambda_d\pi}{H}) \approx \frac{\Lambda_d\pi}{H}$ since $H \gg \Lambda_d$, and $\Gamma(2-\frac{2\Lambda_d}{H}) \approx \Gamma(2) = 1$, we get the final form for the isocurvature power spectrum at the pivot scale,

$$P(k_P) = \frac{f_d^2}{\langle f\rangle^2}\frac{2\Lambda_d}{H}e^{\frac{-2\Lambda_d}{H}N_P}. \tag{6.10}$$

This can be rewritten using the dimensionless β_n (see Eq. (5.8)),

$$P(k_P) = \frac{f_d^2}{\langle f \rangle^2} 2\beta_d \frac{H^2}{F_a^2} e^{-2\beta_d \frac{H^2}{F_a^2} N_P}. \tag{6.11}$$

From (6.11) it is clear that the important factor determining the value of the power spectrum is the dimensionless $\frac{H}{F_a}$. The current data gives an upper bound on the isocurvature between dark matter and CMB photons, $P(k_P) \lesssim 0.040 P_\zeta(k_P)$ [41], which corresponds to

$$P(k_P) \lesssim 8.8 \times 10^{-11}. \tag{6.12}$$

Finally, it is important to note that there are originally two different Hubble parameters entering equation (6.11). The e-fold number N_P features H_I, the inflationary Hubble parameter. The other Hubble parameter H originates from our Fokker-Planck equation, but since it describes the evolution of the axion quantum field in a de Sitter universe during inflation, the two can indeed be assumed to be a same constant value.

6.2 Dark matter density parameter

Having found the mathematical form of our axion isocurvature power spectrum (6.11), we need to link its three free parameters – F_a, H, and α – to each other, in order to derive numerical values that can be compared to existing data and research (we note that α affects the power spectrum through the eigenvalue equation (5.7)). In this Dissertation, we assume that the strongest constraint on the various axion parameters is the isocurvature constraint introduced above (6.12). In addition, we use the well-known dark matter density parameter to get a further relation [48],

$$\Omega_{DM} h^2 \simeq 0.12\,. \tag{6.13}$$

In the following we will assume that the axion particles are created purely through the realignment mechanism, and account for the total dark matter density. However, we need to adapt the

available calculations on the axion energy to accommodate for our density function (3.3). A rigorous treatment involving the quark masses and the QCD breaking scale can be found in [49], and for a simplified version using the critical time when the axion field starts oscillating, as well as the conservation of axions per comoving volume, the reader is referred to [15]. As our density function (3.3) contains a logarithmic anharmonic part, we use the version for Ω_{DM} as presented in [10]. This relies on [50, 51, 52], which form the basis for any axion energy density calculations. For completeness, we note that the scenario we use from [10] initially assumes a homogeneous misalignment angle at the end of inflation, which is common to most models where the PQ symmetry is broken during inflation. However, using our definition for the energy density (3.3) and the stochastic method, we can directly write the result from [10] as

$$\Omega_{DM}h^2 = 0.12 \times 2\frac{\langle f_{\text{full}}(\phi)\rangle}{F_a^2 m_a^2}\left(\frac{F_a}{5\times 10^{11}\text{ GeV}}\right)^{\frac{7}{6}}, \tag{6.14}$$

where the coefficient $F_a^2 m_a^2$ of our density function $f_{\text{full}}(\phi)$ cancels out. The factor $\langle f_{\text{full}}(\phi)\rangle$ is where the stochastic approach comes into play, replacing the assumption of a homogeneous misalignment angle. It is the expectation value for the energy density function, and can be expressed as

$$\langle f(\phi)\rangle = \int_{-\pi}^{\pi} P_{eq} f(\phi) d\phi\,, \tag{6.15}$$

with P_{eq} defined in (4.19). It is worth noting that Eq. (6.14) includes the assumption that $H_I \gg \Lambda_{QCD}$ [53], and hence it does not depend on the inflationary Hubble parameter H_I, even though this would theoretically be expected as the axion density is strongly influenced by the inflationary fluctuations. This assumption should be carefully investigated for the different scenarios presented. The final relation restricting F_a comes from combining Eq. (6.14) with the experimental value (6.13), and is used in the rest of the calculations to find a value of F_a for a given α.

6.3 Approximation schemes

In addition to the full stochastic treatment for the axion presented in Section 5, the corresponding calculations were also computed for two different approximation schemes: the harmonic approximation and a mixed treatment with the harmonic spectrum but the full density function. These approximation schemes give further insight into the role of the various factors in our calculations.

6.3.1 Harmonic treatment

For the harmonic treatment, we approximate both the cosine axion potential (2.11) and the axion energy density function with a quadratic form. Hence, we use

$$V(\phi) = \frac{1}{2} V_0 \phi^2 \tag{6.16}$$

for the potential, and the quadratic energy density $f_{\text{harm}}(\phi)$ (3.2), as presented in Section 3.3. Then following the steps in Section 5.1 to find the eigenvalue equation for the quadratic potential (6.16), we find the operator

$$\tilde{D}_a = \frac{1}{2}\frac{\partial^2}{\partial a^2} - \frac{1}{2}\left[\left(\frac{4\pi^2}{3H^4}\frac{V_0}{F_a^2}a\right)^2 - \frac{4\pi^2}{3H^4}\frac{V_0}{F_a^2}\right], \tag{6.17}$$

where we remember the relation (2.6) between $\phi(x)$ and $a(x)$. This then gives the harmonic eigenvalue equation,

$$\frac{\partial^2 \psi_n}{\partial \phi^2} - \left[\frac{16\pi^4}{9}\alpha^2\phi^2 - \frac{4\pi^2}{3}\alpha\right]\psi_n = -8\pi^2\beta_n\psi_n, \tag{6.18}$$

with α (5.4) and β_n (5.8) defined as before. This leads to the energy density equation (6.14) becoming

$$\Omega_{DM}h^2 = 0.12 \times 2\frac{\langle f_{\text{harm}}(\phi)\rangle}{F_a^2 m_a^2}\left(\frac{F_a}{5\times 10^{11}\text{ GeV}}\right)^{\frac{7}{6}} \tag{6.19}$$

in the quadratic scheme, using $f_{\text{harm}}(\phi)$ (3.2) and the eigenvalue equation (6.18) to find $\langle f_{\text{harm}}(\phi)\rangle$ from ψ_0 (see Eqs. (6.15) and (4.19)). Again, the experimental value for $\Omega_{DM}h^2$ (6.13) can be used to constrain F_a.

6.3.2 Mixed treatment

The mixed approximation involves the quadratic eigenvalue equation (6.18), thus having a harmonic spectrum, but for the axion energy density it uses the full density function $f_{\text{full}}(\phi)$ (3.3). Hence, it is expected to give more accurate results than the harmonic approximation, being a middle ground between the harmonic and the full stochastic treatment. To avoid confusion, we emphasise that the mixed treatment uses Eq. (6.14) just as the full treatment, but the eigenfunction ψ_0 entering the equation through (6.15) differs from the full treatment, as it comes from the harmonic eigenvalue equation (6.18).

6.4 Axion decay constant F_a

Since the parameter α (5.4) controls the eigenvalue equation (5.7) of our stochastic method (for the quadratic approximation Eq. (6.18)), we compute our results by fixing α and constraining the axion decay constant F_a afterwards through the assumption that all dark matter must have been created from axions (see Eqs. (6.14) and (6.13)). Figure 16 demonstrates the obtained range of F_a values for the full treatment (in blue) and the approximation schemes. The dots represent the calculated data points and they are joined by a second order interpolation method. We first note that the range of found F_a values, $\sim 10^{11}$-10^{15} GeV, needed to explain the dark matter abundance for a wide range of α values, corresponds well to the range of values found in literature. For example, [29] gives a range of $10^9 \lesssim F_a \lesssim 10^{17}$ GeV stating that F_a is bounded from below by supernova cooling and from above by black hole superradiance. Other references constrain the QCD axion upper limit further to $F_a \lesssim 10^{12}$ GeV through arguments on the fine-tuning of the misalignment angle, see e.g. [47, 14]. Next we observe from Fig. 16 that for large α

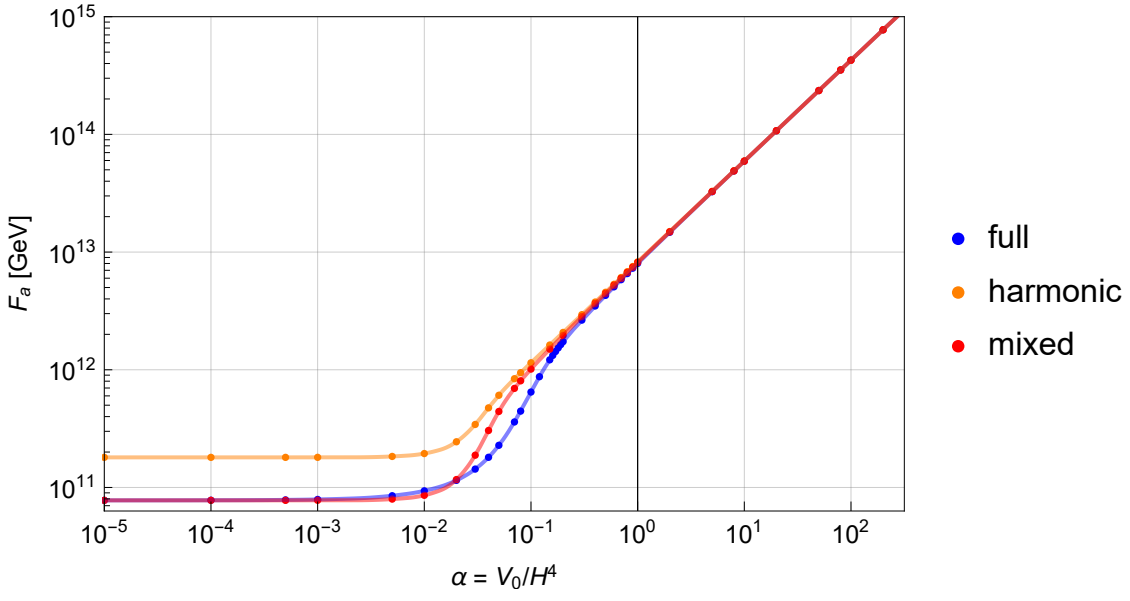

Figure 16: The axion decay constant F_a needed to explain the observed dark matter abundance as a function of the parameter α. A second order interpolation has been used to join the calculated data points (represented by the dots). The relevant equations are (6.14) for the full and mixed, and (6.19) for the harmonic treatment.

($\alpha \gtrsim 1$), both approximations converge to the same limit as the full treatment. This is expected since it is the case when $V_0 \gg H$, i.e. the energy density of the axion is low compared to its potential. Hence, the axion will be found close to the bottom of the potential, where the harmonic approximation is accurate for both the axion energy density (3.2) and its potential (6.16), making the corresponding factors in the mixed and full treatment become quadratic.

On the other hand, for $\alpha \lesssim 1$ the approximations show a clear difference from the full treatment. Figure 16 demonstrates that around $\alpha \sim 0.1$ the mixed approximation (in red) follows first the harmonic one (in orange) before converging back to the full treatment (in blue). This is because the mixed treatment includes the harmonic spectrum, as discussed in Section 6.3.2. As long as the quadratic approximation for the axion potential (6.16) is valid, and the logarithmic factor does not dominate the energy density (3.3), the mixed treatment follows the harmonic one closely. The full treatment differs from these two because the anharmonic part of its potential becomes significant. In the following analysis, we call this regime where all three curves are distinct a transition region. This is the regime where $V_0 \sim H^4$, i.e. the axion potential is comparable to its energy density, the free-field approximations break down, and new dynamics are observed.

For small α, $V_0 \ll H^4$, we observe the other free field approximation, the freely travelling wave. The axion has so much energy that it does not "see" the potential. Mathematically, the potential term which is multiplied by α does not affect the eigenvalue equation (5.7) anymore, and we essentially recover a one-dimensional Helmholtz equation which has well-known analytical solutions. Since the full and mixed treatments differ only in their potential (see Section 6.3), they converge as would be expected. We recall that the mixed treatment agrees with the full one also at large α values, due to the harmonic convergence, and hence is a good approximation for axion dynamics outside the transition region. The reason the harmonic approximation is clearly off for small α in Fig. 16 is that its energy density function is the harmonic approximation (3.2), which is invalid in this limit. We also note that the convergence of F_a for low α in Fig. 16 seems to imply that there exists a low bound on F_a, below which our axion model cannot account for the whole of the dark matter anymore. On the other hand, there seem to be no such upper bound.

6.5 Power spectrum and Hubble parameter H

6.5.1 QCD axion and low-scale inflation

Having constrained F_a as a function of α with the known dark matter density parameter (see Section 6.4), we can directly calculate the zero temperature asymptotic mass of the QCD axion (discussed in Section 2.1.3), from [17] we find

$$m_a = 5.7 \times 10^{-6} \left(\frac{10^{12}\ \text{GeV}}{F_a} \right) \text{eV}. \tag{6.20}$$

This equation is derived from the bound on V_0 (2.12) for the QCD axion. As fixing α fixes both F_a and m_a, the Hubble parameter H is then directly defined from α (5.4) with the canonical form of the axion potential amplitude, $V_0 = F_a^2 m_a^2$,

$$\alpha = \frac{F_a^2 m_a^2}{H^4}. \tag{6.21}$$

The found values of H for the QCD axion are demonstrated in Figure 17. Here we use H instead of H_I to emphasise that the found Hubble value is the one from the stochastic method, even though it is assumed to correspond to the inflationary Hubble parameter, as discussed at the end of Section 6.1. From Fig. 17 it is clear that the Hubble values predicted for our QCD axion model, of order $\sim 10^{-1}$ GeV, are really small compared to the current upper bound on the inflationary Hubble parameter, which is constrained to be lower than $\sim 10^{14}$ GeV for a single-field inflationary model with slow-roll [54]. While the inflationary Hubble parameter does not have an experimental lower bound, a low-scale inflation model like the one found here is hard to match with other theoretical requirements from the inflationary epoch. The QCD axion in the context of low-scale inflation has been studied in [53], and our values match well their predicted range, providing one way to test our model. We also observe that these Hubble parameter values are of the same order of magnitude as the QCD breaking scale Λ_{QCD}. This implies that for this axion

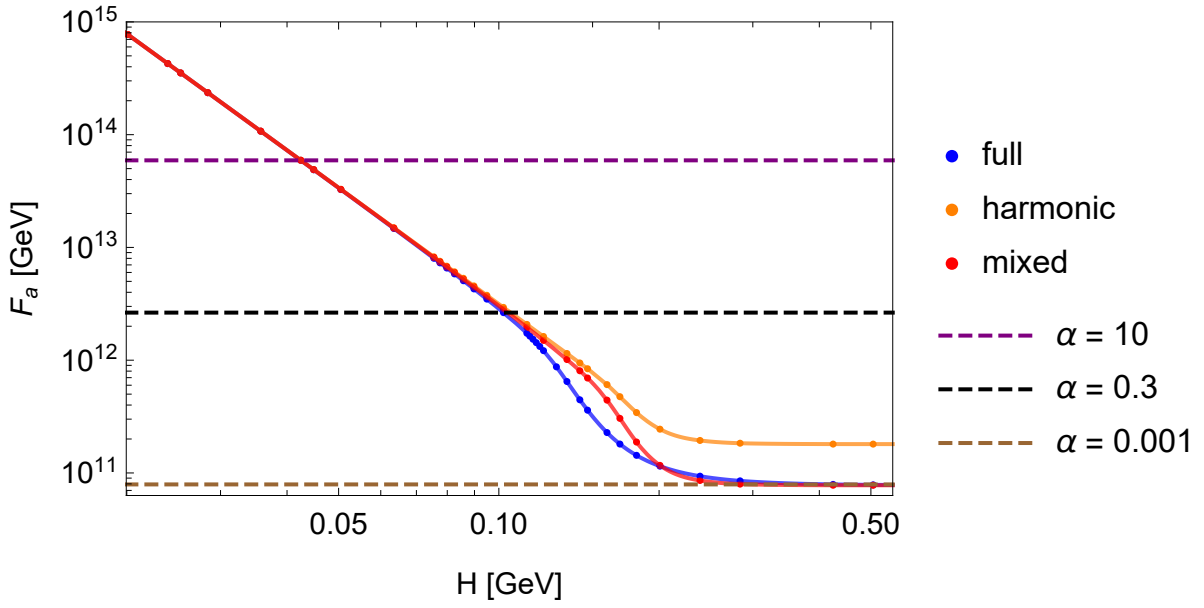

Figure 17: The Hubble parameter for the QCD axion calculated from (6.21), which indicates a low-scale inflation model. Each dot is a data point, and second-order interpolation has been used to join them. The transition region is observed in the α range 0.001-0.3.

model the explicit symmetry breaking of $U(1)_{PQ}$ might happen already during inflation, with potentially observable consequences. It is important to note that this scenario also breaks the assumption about the magnitude of the Hubble parameter used in calculating Ω_{DM}.

From Figure 17 we notice again the free-field behaviours where the full and mixed treatments agree, as well as how the harmonic approximation breaks down for small α. In the middle the transition region appears, approximately in the α range 0.001-0.3 (see Section 6.6). As expected, the mixed treatment follows again first the harmonic curve before converging to the full one. As F_a decreases, we notice a converging pattern, due to the fact that F_a has a lower bound as demonstrated in Fig. 16, and hence from (6.21) we see that $H \to \infty$ as $\alpha \to 0$. The physicality of this behaviour is open to further study, but if the results apply for small enough α, we conclude that the QCD axion can also predict conventional inflationary scales (see Section 7.3 for a discussion on the numerical errors at small parameter values). This would be the case of a highly energetic axion (see Section 5.3.1).

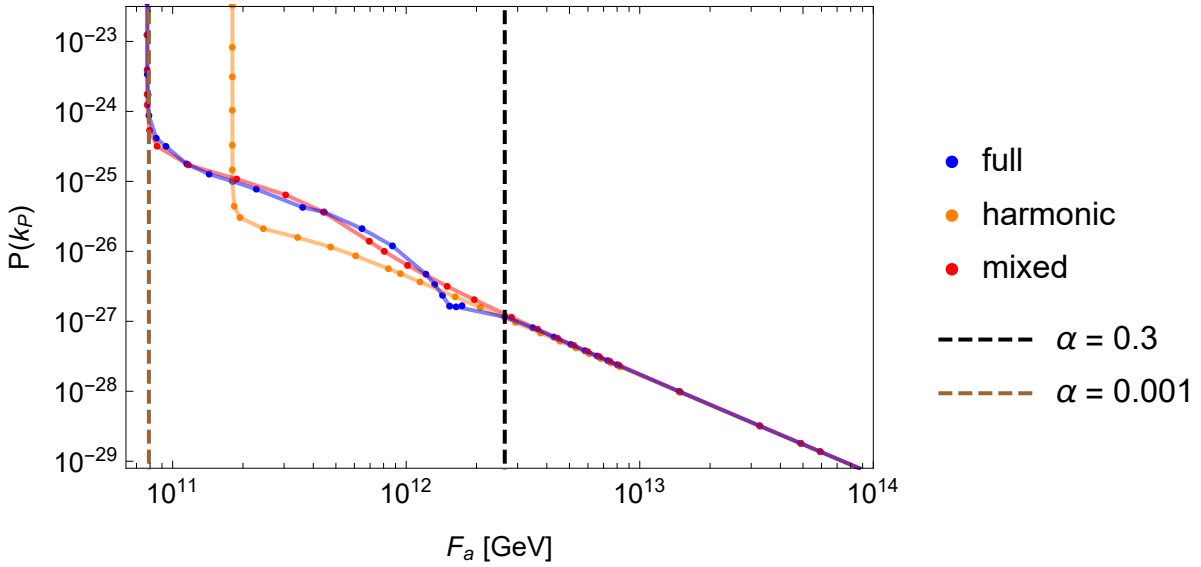

Figure 18: The power spectrum of the QCD axion as a function of F_a. It is negligible compared to the current observational bound (6.12) for the isocurvature contribution.

Having found these values for the Hubble parameter, we can next turn to investigate whether the corresponding power spectrum, calculated from Eq. (6.11), obeys the allowed bound. This is shown in Figure 18, which demonstrates that the power spectrum of the QCD axion is smaller than the isocurvature bound (6.12) by many orders of magnitude, at least for $\alpha \gtrsim 0.001$. This makes our axion theory a potential dark matter candidate from an isocurvature point of view. However, a negligible isocurvature compared to the current observational limit makes it hard to test this theory experimentally. From Figure 18 we also observe the asymptotic behaviour of the power spectrum for low α, which is a direct consequence of the behaviour of H in Fig. 17. Assuming this behaviour is physical, the power spectrum of the QCD axion could theoretically reach the current isocurvature bound, in the limit of vanishing α. Finally, from the power spectrum in Figure 18 we notice a clear edge in the transition region for the full treatment (in blue), below $\alpha \sim 0.3$, which is not present in the mixed treatment (in red), even though it follows the full one quite closely. This will be investigated in Section 6.6.

6.5.2 Inflationary scales for general axion

The mass of the general axion (see Section 2.1.4) depends on the underlying extended theory, and hence we do not use it in the context of this Dissertation. Instead, assuming an arbitrary but constant amplitude V_0, we use the isocurvature bound to give a constraint on the inflationary Hubble parameter for the general axion scenario. This is done by setting the power spectrum (6.11) to the maximum isocurvature value in Eq. (6.12), which gives an upper limit for H_I. The results are demonstrated in Figure 19, where the purple line gives a first-order interpolation for the values calculated from the full treatment, showing the transition region as a sharp edge around $F_a \sim 10^{12}$ GeV. These values of H_I are much closer to common inflationary scales than the low-scale values found in Fig. 17 for the QCD axion. For demonstration purposes, the right y-axis shows the mass of the QCD axion in eV corresponding to the decay constant F_a (see Eq. (6.20)). We observe that these values for the axion mass fit within the upper bound $m_a \lesssim 10^{-4}$ eV

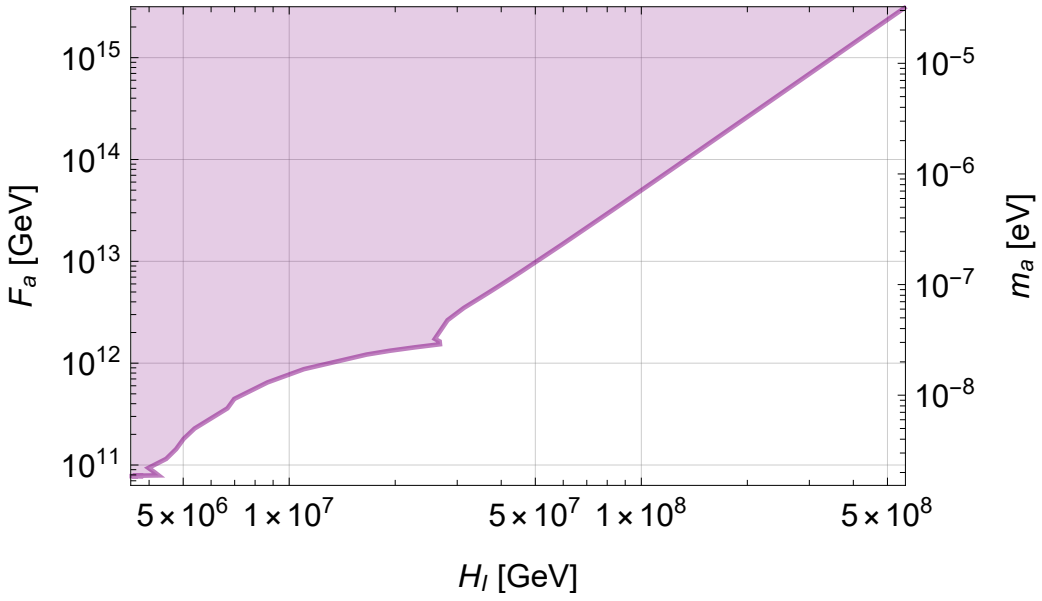

Figure 19: Allowed values (in purple) for the inflationary Hubble parameter H_I for a general axion. A first-order interpolation for the calculated points has been used, making the transition region around $F_a \sim 10^{12}$ GeV visible. The left y-axis shows the decay constant F_a, while the right y-axis gives the corresponding mass for the QCD axion.

for non-thermally produced QCD axions [55]. For completeness, we also note that implementing the isocurvature bound actually results in two boundary values for H_I for a given F_a. However, as the other one is much larger than the well-established upper bound on the inflationary Hubble parameter, we choose to dismiss it as unphysical and concentrate on the lower value, which is pictured in Fig. 19.

We can compare this predicted parameter space with existing research, for example with the bounding regions in [56], which match our boundary for H_I in Fig. 19 closely, both being limited by the isocurvature bound. The fact that our stochastic method gives a boundary for H_I that is not only in the correct order of magnitude from an inflationary point of view, but also a close fit to results from previous research, is a validation of the approach we have taken in this Dissertation to calculate the axion two-point correlator. In addition, our findings for the upper limit of H_I in Fig. 19 reveal unexplored dynamics in the transition region, which will be further discussed in the next section. Overall, we conclude that the scale of H_I that is predicted for our general axion is more compatible with current inflationary models, making it a more physical scenario than the QCD axion.

Finally, we note that while the general axion scenario relaxes the QCD bound on V_0 and allows the inflationary scales pictured in Fig. 19, it brings more complexity to other axion parameters as well. For example, string axions permit decay constants in the GUT scale $F_a \sim 10^{16}$ GeV [29]. In addition, in string axion models the dark matter parameter Ω_{DM} depends strongly on the inflationary scale H_I [20], which might be the case for other general axion types as well, and hence should be taken into account for any rigorous treatment of a specific general axion model. The final part of the results consists of studying the new dynamics emerging from the stochastic approach in the transition region where both free-field approximations break down.

6.6 The transition region

This subsection investigates the novel feature captured by our stochastic treatment, the transition region, found e.g. in Figure 17 to be approximately in the α range 0.001-0.3. We start by picturing in Figure 20 a zoomed in version of Fig. 19 but now with the approximation schemes (see Section 6.3), demonstrating the transition region where the harmonic and mixed approximations break down in our F_a-H_I parameter plane. There is a clear edge around $\alpha \sim 0.2$ in the full treatment (in blue) that is not observed in the approximation schemes. This is particularly interesting as the corresponding $F_a \sim 10^{12}$ GeV is a conventional value for the QCD axion decay constant. From Figure 20 we also note how the computational numerical inaccuracy becomes significant for low values of F_a, as all the three curves exhibit random non-smooth patterns.

The sharp behaviour in the full treatment in Fig. 20 arises from the calculation of the isocurvature power spectrum (6.11), where we need to choose the leading eigenlevel that gives the dominant contribution f_d to the spectral expansion of the two-point correlator (4.29) (see the discussion on

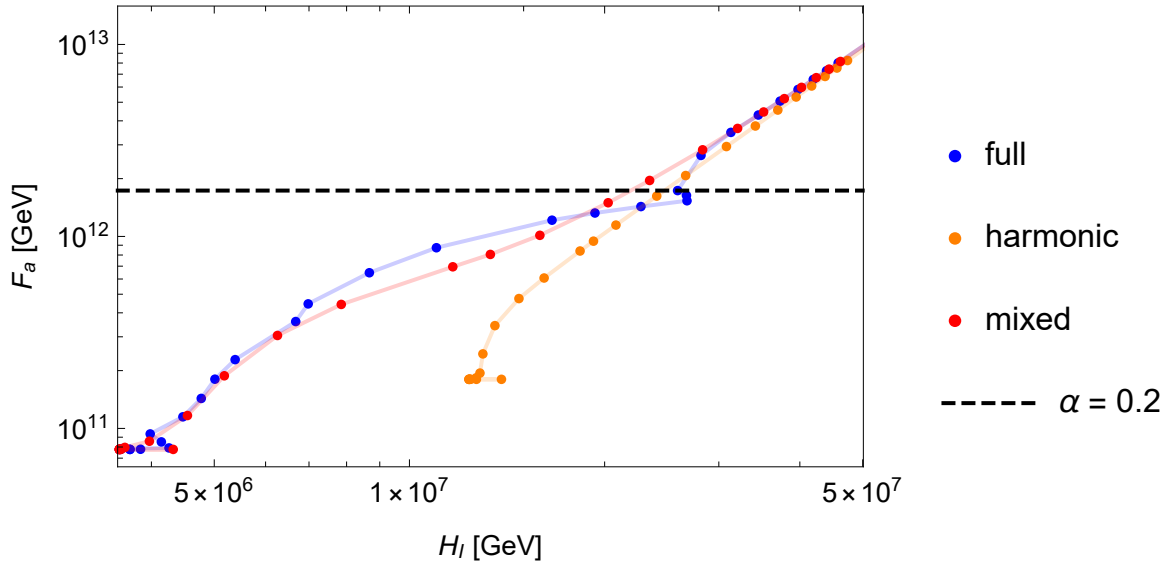

Figure 20: The transition region in our F_a-H_I parameter plane showing the upper bound on H_I for a general axion. The clear edge in the full treatment (in blue) can be observed close to $\alpha \sim 0.2$.

the eigenlevels at the end of Section 4.3.4). We use the level that gives the smallest H_I, i.e. the strictest upper bound on the Hubble parameter (or alternatively, the largest value for the power spectrum $P(k_P)$). It was observed that the second largest expansion term usually gave a result that was differing from the leading term by at least one order of magnitude, hence validating our approximation in the isocurvature correlator calculation (6.6) to use only the leading term of the spectral expansion. In our case, the significant contributions come from the first two excited eigenlevels, and in the transition region the balance between them changes.

In the full treatment, the leading eigenlevel is the first one for $\alpha \lesssim 0.2$, which corresponds to a non-perturbative state. However, for $\alpha \gtrsim 0.2$, the leading eigenlevel is the second one with a perturbative eigenfunction. We recall that there are two eigenfunctions per level, but only one of them has the correct parity to give a non-zero spectral coefficient (4.27), as both the ground state and the energy density function are even. The dynamics between the first two excited eigenlevels is demonstrated in Figure 21, where the purple data points correspond to the first eigenlevel while

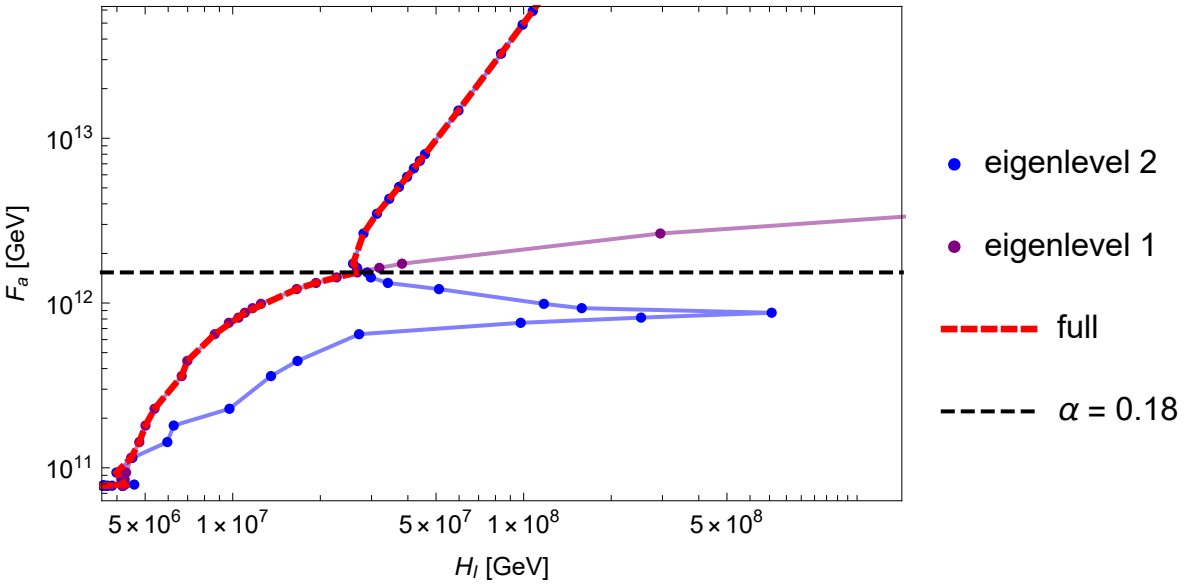

Figure 21: The bounds for H_I, calculated using the power spectrum (6.11), from eigenlevel 1 (in purple) and eigenlevel 2 (in blue) of the stochastic method. The red dashed line indicates the combined boundary for H_I, which is evaluated based on the most stringent constraint.

the blue ones correspond to the second one. This is another zoomed in version of Fig. 19, focused on the transition region, now revealing the contributions of the two dominating eigenlevels in addition to the combined boundary for H_I, shown by the red dashed line (which is presented in blue in Fig. 20 and in purple in Fig. 19). From a cosmological point of view, we see that the first eigenlevel has a red spectrum, since it dominates at long distances (the Hubble parameter has natural units of 1/length). The second eigenlevel, dominating at short distances, corresponds thus to a blue spectrum.

In contrast, in the harmonic approximation the leading level is always the first excited eigenlevel, producing a smooth behaviour. The leading term of the mixed approximation does include a transition from one eigenlevel to the other, but it is much smoother than the transition of the full treatment. From Fig. 21 we observe that while the first eigenlevel seems to exhibit a smooth behaviour, the second one has a really sharp edge below $\alpha = 0.18$. To understand this feature, we investigate the spectral coefficients f_n (from Eq. (4.27)) and the eigenvalues β_n (calculated from (5.7)) entering the power spectrum (6.11) as a function of α, which is shown in Figure 22. We observe that the spectral coefficient f_n of the second eigenlevel (in blue) changes sign around $\alpha \approx 0.12$, which results in the sharp behaviour in Fig. 21 as f_n^2 effectively goes to zero (see Eq. (6.11)). This is understood when remembering that the actual physical quantity that is behind the spectral coefficient is the matrix element $f_n = \langle 0|f|n\rangle$, the sign of which is arbitrary. However, as this singular behaviour in the second eigenlevel arises when it is no longer the dominant level, as demonstrated in Fig. 21, it does not affect the overall results and remains a curiosity.

The power spectrum (6.11) is completely determined by the dynamics between the spectral coefficient and the corresponding eigenvalue. While f_n^2 provides an overall multiplicative factor, β_n both multiplies the power spectrum and enters the exponential in (6.11). However, β_n will have only a small impact on the exponential term, which contains numerically much larger parameters (H_I, F_a), and hence its overall multiplicative effect is more significant. For $\alpha \gtrsim 0.18$, the spectral coefficient f_n^2 in Fig. 22 is approximately the same for both eigenlevels (recalling that Fig. 22 shows f_n), but the β_n of the second eigenlevel (in blue) is clearly larger, giving the tightest

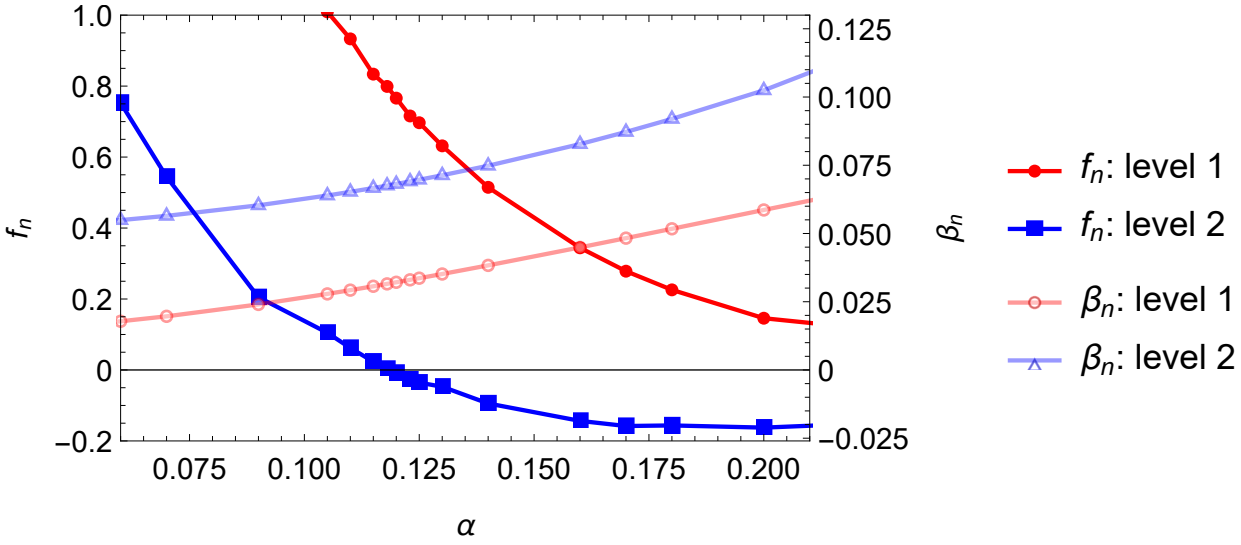

Figure 22: The spectral coefficients f_n and the eigenvalues β_n contributing to the power spectrum (6.11) as a function of α in the transition region. The first eigenlevel is shown in red, and the second one is in blue.

constrain on H_I. With a larger value of H_I, the contribution from the second eigenlevel would alone exceed the isocurvature bound. On the other hand, for $\alpha \lesssim 0.18$, the spectral coefficients start to differ with f_n^2 of the second level being significantly lower. Hence, the difference between the spectral coefficients f_n dominates the power spectrum values and now it is the first eigenlevel that gives the most stringent constrain on H_I, as its spectral coefficient is much larger.

To give a physical interpretation to this behaviour, we explore the perturbativeness of the eigenstates corresponding to the two eigenlevels in Fig. 22. As mentioned previously, the eigenstate of the second level, dominating at larger α, is perturbative. This makes sense as the harmonic approximation is valid in this limit, and it sees only the perturbative states centred around the minimum of the potential. However, on the small α side of the transition region, the first eigenlevel becomes dominant, and the corresponding eigenfunction is non-perturbative. This is exactly the regime where the harmonic approximation breaks down, as it does not take into account this non-perturbative state, and the full stochastic treatment is needed. The reason for the dominance of this non-perturbative state is a higher tunnelling probability with the ground state, as the axion is no longer confined to the bottom of its potential (see discussion in Section 5.3.2).

7 Discussion

In this Dissertation, the cosmological consequences of the stochastic axion were studied. In the calculations, it was assumed that axions would be the only dark matter species, and we use the dimensionless parameter α throughout the results to characterise the dynamics between the axion energy and its potential. In addition to the full stochastic approach, the final calculations were computed for both the harmonic and the mixed treatment to test the accuracy of the stochastic method. The final results span two different levels. The mathematical part includes calculating the axion isocurvature power spectrum (see Eq. (6.11)), while the cosmological part involves predictions on the axion decay constant F_a, the Hubble parameter H, and the isocurvature component (Sections 6.4 and 6.5). The bound for the Hubble parameter in the general axion scenario is particularly interesting as it reaches conventional inflationary scales (see Figure 19).

The axion two-point correlator and its isocurvature component have not been previously calculated using the stochastic approach. Hence, the results in this Dissertation provide a new input to current axion research. Especially the transition region (see Figure 21) emerging from the stochastic method reveals new aspects in the dynamics of the cosmological axion. This is the regime where neither of the free-field limits is valid, and we conclude that only the full stochastic treatment gives accurate results. In this section, we discuss and draw together these results, highlighting the significance of the stochastic approach (7.2), the limitations of our axion model (7.3), and its consequence for the axion theory (7.1).

7.1 Consequence for axion theory

The results found for the axion decay constant F_a, constrained through the dark matter density parameter, fit well within existing literature values. Implementing the found range of F_a for the QCD axion, we found a low-scale inflation model. While improbable in the light of current research, this scenario cannot be directly cast out as unphysical, as there is currently no experimental lower bound on H_I. The isocurvature power spectrum of the QCD axion was computed with these low-scale H_I values and was found negligible compared to the current isocurvature

bound. It is however worth noting that in the limit of vanishing α, the QCD axion has an asymptotic behaviour with the potential to reach conventional inflationary scales.

For the general axion, we used the current observational isocurvature bound to find a limiting value for the inflationary Hubble parameter. The upper bound for H_I from our theory reproduces results from common axion literature, belonging to the conventional inflationary scales. The general axion scenario is therefore easier to combine with other requirements from the inflationary epoch, in addition to opening up the possibility to merge axion theory into physics beyond the Standard Model.

7.2 Significance of the stochastic method

The axion correlator has commonly been computed through the linear approximation. The stochastic behaviour in the axion quantum field has previously been taken into account only in the evaluation of the axion scalar field one-point distribution (see [13]), but in this Dissertation we have computed the whole stochastic spectrum, which is beneficial for multiple reasons. Firstly, by working with probability distributions it avoids the fine-tuning problem of the misalignment angle (discussed for example in [57]), which assumes a homogeneous misalignment angle for the whole axion field if the PQ symmetry is broken during inflation.

Secondly, the stochastic treatment of the cosmological axion reveals the non-linear effects responsible for the transition region, which was found to be within $0.001 \lesssim \alpha \lesssim 0.3$. In this region the balance between the energy density and the potential of the axion changes, rendering the free-field approximations invalid. This physical behaviour is reflected in the dynamics occurring between the first two excited eigenlevels, which dominate the spectral expansion of the two-point correlator (see Figure 21). The eigenstate of the first level is non-perturbative, while the second one is perturbative, which is significant since the validity of the harmonic approximation can be directly derived from the perturbativeness of these eigenstates. Consequently, it was found that the linear approximation breaks down for $\alpha \lesssim 0.18$, where the non-perturbative state has the dominating contribution due to the higher tunnelling probability at lower α. The potentially ob-

servable cosmological signatures of the axion dynamics at play within the transition region form an area for further research.

7.3 Limitations of the model

As the axion eigenvalue equation (5.7), which is a second-order differential equation, was evaluated numerically in Mathematica, errors arise especially for small parameter values from the finite difference scheme used. The numerical evaluation forms the main error source for the results presented in this Dissertation. It was commonly observed during the computation process that the eigenspectrum for really small α seemed to be unreliable. Hence, to quantify the computational level of accuracy, the calculations should be done with varying numerical methods, preferably manually using e.g. the overshoot/undershoot method. Another way to validate the results would be to repeat the calculations for a different range of the misalignment angle, e.g. for $[0, 2\pi]$, which should give the same numerical results due to the periodicity of the axion potential.

Another important point to notice is that we have assumed in this Dissertation constant values for the inflationary Hubble parameter H_I and the axion mass m_a, which in reality are temperature-dependent. To refine our axion model, this variation should be taken into account. Another potential error source is the assumption $H_I \gg \Lambda_{QCD}$ behind the calculation of Ω_{DM}, which should be carefully examined depending on the axion scenario we are considering, especially in the case of low-scale inflation. As this Dissertation provides an overall exploration of the stochastic axion, the different steps in the calculations could be refined to serve a specific axion model, such as the string axion. In addition, several factors such as quantum corrections and present-day axion self-interactions could be considered.

8 Conclusion

The results presented in this Dissertation highlight new aspects of the cosmological axion, emerging from the stochastic approach that has not been previously implemented in the evaluation of the axion isocurvature contribution. Developing these further would enable a deep understanding of the dynamics at play in the transition region, with the potential to predict an experimentally detectable cosmological signature. In addition, it was found that general axion scenarios allow isocurvature components close to the current experimental limit, enabling the refinement of the corresponding models with more accurate data from the CMB. Overall, our results highlight the limitations of existing axion models relying on the common linear approximation.

As dark matter accounts for almost a third of the Universe's energy, its origin is a pressing scientific problem waiting to be solved. With the unexpected signal discovered from the Xenon1T experiment hunting dark matter, this is an exciting time for the global axion community. If the quest for axions ultimately proves to be successful, it would not only revolutionise our understanding of the Universe, but also transform the theoretical work presented in this Dissertation into the physics of the most abundant form of matter in our Universe.

References

[1] M. S. Seigar. *Dark Matter in the Universe*. 2053-2571. Morgan & Claypool Publishers, San Rafael, 2015. DOI: https://doi.org/10.1088/978-1-6817-4118-5.

[2] B. Beltran, M. Kuster, and G. Raffelt (Eds.). *Axions: Theory, Cosmology, and Experimental Searches*, volume 741 of *Lecture Notes in Physics*. Springer, Berlin, 2008. DOI: https://doi.org/10.1007/978-3-540-73518-2.

[3] P. Rincon. Dark matter hunt yields unexplained signal. *BBC News*. Available from: https://www.bbc.co.uk/news/science-environment-53085260, 17th June 2020. [Accessed: 13th September 2020].

[4] E. Aprile, J. Aalbers, F. Agostini, M. Alfonsi, L. Althueser, and F. D. Amaro et al. Observation of Excess Electronic Recoil Events in XENON1T. Arxiv. [hep-ex] 2020. Available from: https://arxiv.org/abs/2006.09721. [Accessed: 21st September 2020].

[5] R. D. Peccei and H. R. Quinn. CP conservation in the presence of pseudoparticles. *Physical Review Letters*, 38(25):1440–1443, 1977. DOI: https://doi.org/10.1103/PhysRevLett.38.1440.

[6] R. D. Peccei and H. R. Quinn. Constraints imposed by CP conservation in the presence of pseudoparticles. *Physical Review D*, 16(6):1791–1797, 1977. DOI: https://doi.org/10.1103/PhysRevD.16.1791.

[7] S. Weinberg. A New Light Boson? *Physical Review Letters*, 40(4):223–226, 1978. DOI: https://doi.org/10.1103/PhysRevLett.40.223.

[8] F. Wilczek. Problem of Strong P and T Invariance in the Presence of Instantons. *Physical Review Letters*, 40(5):279–282, 1978. DOI: https://doi.org/10.1103/physrevlett.40.279.

[9] A. Ringwald. Axions and Axion-Like particles. Arxiv. [hep-ph] 2014. Available from: https://arxiv.org/abs/1407.0546. [Accessed: 21st September 2020].

[10] R. T. Co, E. Gonzalez, and K. Harigaya. Axion misalignment driven to the hilltop. *Journal of High Energy Physics*, 2019(5):1–22, 2019. DOI: https://doi.org/10.1007/jhep05(2019)163.

[11] K. Schmitz and T. T. Yanagida. Axion isocurvature perturbations in low-scale models of hybrid inflation. *Physical Review D*, 98(7), 2018. DOI: https://doi.org/10.1103/PhysRevD.98.075003.

[12] C. Baugh. *Correlation Function and Power Spectra in Cosmology*. In: Encyclopedia of Astronomy & Astrophysics, P. Murdin (Ed.). Institute of Physics Publishing, Bristol, 2000.

[13] P. W. Graham and A. Scherlis. Stochastic axion scenario. *Physical Review D*, 98(3), 2018. DOI: https://doi.org/10.1103/PhysRevD.98.035017.

[14] T. Kobayashi. Cosmological perturbations of axion with a dynamical decay constant. *Journal of Cosmology and Astroparticle Physics*, 2016(8):56, 2016. DOI: https://doi.org/10.1088/1475-7516/2016/08/056.

[15] L. D. Duffy and K. van Bibber. Axions as dark matter particles. *New Journal of Physics*, 11(10): 105008, 2009. DOI: https://doi.org/10.1088/1367-2630/11/10/105008.

[16] M. Beltran, J. Garcia-Bellido, and J. Lesgourgues. Isocurvature bounds on axions revisited. *Physical Review D, Particles Fields*, 75(10), 2007. DOI: https://doi.org/10.1103/PhysRevD.75.103507.

[17] A. Arvanitaki, S. Dimopoulos, M. Galanis, L. Lehner, J. O. Thompson, and K. Van Tilburg. Large-misalignment mechanism for the formation of compact axion structures: Signatures from the QCD axion to fuzzy dark matter. *Physical Review D*, 101(8):083014, 2020. DOI: https://doi.org/10.1103/PhysRevD.101.083014.

[18] S. Bottaro and E. Meggiolaro. QCD axion and topological susceptibility in chiral effective Lagrangian models at finite temperature. *Physical Review D*, 102(1):014048, 2020. DOI: https://doi.org/10.1103/PhysRevD.102.014048.

[19] Sz. Borsanyi, Z. Fodor, K. H. Kampert, S. D. Katz, T. Kawanai, and T. G. Kovacs et al. Lattice QCD for cosmology. Arxiv. [hep-lat] 2016. Available from: https://arxiv.org/abs/1606.07494. [Accessed: 21st September 2020].

[20] P. Fox, A. Pierce, and S. Thomas. Probing a QCD String Axion with Precision Cosmological Measurements. Arxiv. [astro-ph] 2004. Available from: https://arxiv.org/abs/hep-th/0409059. [Accessed: 21st September 2020].

[21] R. Balkin, J. Serra, K. Springmann, and A. Weiler. The QCD axion at finite density. *Journal of High Energy Physics*, 2020(7):1–50, 2020. DOI: https://doi.org/10.1007/JHEP07(2020)221.

[22] H. Risken. *The Fokker-Planck equation: Methods of solution and application.* Springer series in synergetics 18. Springer, Berlin, 1996. (Second edition). DOI: https://doi.org/10.1007/978-3-642-61544-3.

[23] A. E. Siegman. Simplified derivation of the Fokker-Planck equation. *American Journal of Physics*, 47(6):545, 1979. DOI: https://doi.org/10.1119/1.11783.

[24] A. A. Starobinsky and J. Yokoyama. Equilibrium state of a self-interacting scalar field in the de Sitter background. *Physical Review D, Particles and fields*, 50(10):6357, 1994. DOI: https://doi.org/10.1103/PhysRevD.50.6357.

[25] M. Feix, J. Frank, A. Pargner, R. Reischke, B. M. Schäfer, and T. Schwetz. Isocurvature bounds on axion-like particle dark matter in the post-inflationary scenario. *Journal of Cosmology and Astroparticle Physics*, 2019(05):021–021, 2019. DOI: https://doi.org/10.1088/1475-7516/2019/05/021.

[26] Paolo Gondolo and Luca Visinelli. Axion cold dark matter in view of BICEP2 results. *Physical Review Letters*, 113(1):011802, 2014. DOI: https://doi.org/10.1103/physrevlett.113.011802.

[27] J.-H. Huh. Update of axion CDM energy density. *AIP Conference Proceedings*, 1078(1):575–577, 2008. DOI: https://doi.org/10.1063/1.3052032.

[28] A. Ringwald. Alternative dark matter candidates: Axions. From: Proceedings of the Neutrino Oscillation Workshop (NOW2016), p. 81. Arxiv. [hep-ph] 2016. Available from: https://arxiv.org/abs/1612.08933. [Accessed: 21st September 2020].

[29] D. J. E. Marsh. Axion cosmology. *Physics reports*, 643:1–79, 2016. DOI: https://doi.org/10.1016/j.physrep.2016.06.005.

[30] E. Komatsu, J. Dunkley, M. R. Nolta, C. L. Bennett, B. Gold, and G. Hinshaw et al. Five-year Wilkinson Microwave Anisotropy Probe observations: Cosmological interpretation. *The Astrophysical Journal Supplement Series*, 180(2):330–376, 2009. DOI: https://doi.org/10.1088/0067-0049/180/2/330.

[31] D. H. Lyth. A limit on the inflationary energy density from axion isocurvature fluctuations. *Physics Letters B*, 236(4):408–410, 1990. DOI: https://doi.org/10.1016/0370-2693(90)90374-F.

[32] M. Kawasaki, E. Sonomoto, and T. T. Yanagida. Cosmologically allowed regions for the axion decay constant F_a. *Physics Letters B*, 782:181–184, 2018. DOI: https://doi.org/10.1016/j.physletb.2018.05.014.

[33] A. A. Starobinsky. Stochastic de Sitter (inflationary) stage in the early universe. *Lecture Notes in Physics*, 246:107–126, 1986. DOI: https://doi.org/10.1007/3-540-16452-9_6.

[34] T. Markkanen and A. Rajantie. Scalar correlation functions for a double-well potential in de Sitter space. *Journal of Cosmology and Astroparticle Physics*, 2020(03):049, 2020. DOI: https://doi.org/10.1088/1475-7516/2020/03/049.

[35] T. Markkanen, A. Rajantie, S. Stopyra, and T. Tenkanen. Scalar correlation functions in de Sitter space from the stochastic spectral expansion. *Journal of Cosmology and Astroparticle Physics*, 2019 (08), 2019. DOI: https://doi.org/10.1088/1475-7516/2019/08/001.

[36] V. K. Onemli. Vacuum fluctuations of a scalar field during inflation: Quantum versus stochastic analysis. *Physical Review D, Particles, fields, gravitation, and cosmology*, 91(10), 2015. DOI: https://doi.org/10.1103/PhysRevD.91.103537.

[37] V. Vennin and A. A. Starobinsky. Correlation functions in stochastic inflation. *The European Physical Journal C, Particles and fields*, 75(9):1–20, 2015. DOI: https://doi.org/10.1140/epjc/s10052-015-3643-y.

[38] F. Gautier and J. Serreau. Scalar field correlator in de Sitter space at next-to-leading order in a $1/N$ expansion. *Physical Review D, Particles, fields, gravitation, and cosmology*, 92(10), 2015. DOI: https://doi.org/10.1103/PhysRevD.92.105035.

[39] D. Glavan, T. Prokopec, and A. A. Starobinsky. Stochastic dark energy from inflationary quantum fluctuations. *The European Physical Journal C, Particles and fields*, 78(5):1–17, 2018. DOI: https://doi.org/10.1140/epjc/s10052-018-5862-5.

[40] R. J. Hardwick, V. Vennin, C. T. Byrnes, J. Torrado, and D. Wands. The stochastic spectator. *Journal of Cosmology and Astroparticle Physics*, 2017(10):18, 2017. DOI: https://doi.org/10.1088/1475-7516/2017/10/018.

[41] T. Markkanen, A. Rajantie, and T. Tenkanen. Spectator dark matter. *Physical Review D, Covering Particles, Fields, Gravitation and Cosmology*, 98(12):1, 2018. DOI: https://doi.org/10.1103/PhysRevD.98.123532.

[42] F. Cooper, A. Khare, and U. Sukhatme. Supersymmetry and quantum mechanics. *Physics Reports*, 251(5-6):267–385, 1995. DOI: https://doi.org/10.1016/0370-1573(94)00080-M.

[43] E. Witten. Dynamical breaking of supersymmetry. *Nuclear Physics, Section B*, 188(3):513–554, 1981. DOI: https://doi.org/10.1016/0550-3213(81)90006-7.

[44] F. Cooper and B. Freedman. Aspects of supersymmetric quantum mechanics. *Annals of Physics*, 146 (2):262–288, 1983. DOI: https://doi.org/10.1016/0003-4916(83)90034-9.

[45] E. J. Chun. Axion dark matter with high-scale inflation. *Physics letters B*, 735:164–167, 2014. DOI: https://doi.org/10.1016/j.physletb.2014.06.017.

[46] M. Bernstein and L. S. Brown. Supersymmetry and the Bistable Fokker-Planck equation. *Physical Review Letters*, 52(22):1933–1935, 1984. DOI: https://doi.org/10.1103/PhysRevLett.52.1933.

[47] T. Kobayashi, R. Kurematsu, and F. Takahashi. Isocurvature constraints and anharmonic effects on QCD axion dark matter. *Journal of Cosmology and Astroparticle Physics*, 2013(9):032, 2013. DOI: https://doi.org/10.1088/1475-7516/2013/09/032.

[48] P. A. R. Ade, N. Aghanim, M. Arnaud, M. Ashdown, J. Aumont, and C. Baccigalupi et al. Planck 2015 results. xiii. Cosmological parameters. *Astronomy & Astrophysics*, 594:A13, 2016. DOI: https://doi.org/10.1051/0004-6361/201525830.

[49] K. J. Bae, J.-H. Huh, and J. E. Kim. Updating the axion cold dark matter energy density. *Journal of Cosmology and Astroparticle Physics*, 2008(9):005, 2008. DOI: https://doi.org/10.1088/1475-7516/2008/09/005.

[50] L. F. Abbott and P. Sikivie. A cosmological bound on the invisible axion. *Physics Letters B*, 120 (1-3):133–136, 1983. DOI: https://doi.org/10.1016/0370-2693(83)90638-X.

[51] J. Preskill, M. B. Wise, and F. Wilczek. Cosmology of the invisible axion. *Physics Letters B*, 120 (1-3):127–132, 1983. DOI: https://doi.org/10.1016/0370-2693(83)90637-8.

[52] M. Dine and W. Fischler. The not-so-harmless axion. *Physics Letters B*, 120(1-3):137–141, 1983. DOI: https://doi.org/10.1016/0370-2693(83)90639-1.

[53] F. Takahashi, W. Yin, and A. H. Guth. QCD axion window and low-scale inflation. *Physical Review D*, 98(1), 2018. DOI: https://doi.org/10.1103/PhysRevD.98.015042.

[54] K. Enqvist, R. J. Hardwick, T. Tenkanen, V. Vennin, and D. Wands. A novel way to determine the scale of inflation. *Journal of Cosmology and Astroparticle Physics*, 2018(2):006, 2018. DOI: https://doi.org/10.1088/1475-7516/2018/02/006.

[55] R. Hložek, D. J. E. Marsh, and D. Grin. Using the full power of the cosmic microwave background to probe axion dark matter. *Monthly Notices of the Royal Astronomical Society*, 476(3):3063–3085, 2018. DOI: https://doi.org/10.1093/mnras/sty271.

[56] O. Wantz and E. P. S. Shellard. Axion cosmology revisited. *Physical Review D, Particles Fields*, 82 (12), 2010. DOI: https://doi.org/10.1103/PhysRevD.82.123508.

[57] R. Co, E. Gonzalez, and K. Harigaya. Axion misalignment driven to the bottom. *Journal of High Energy Physics*, 2019(5):1–14, 2019. DOI: https://doi.org/10.1007/JHEP05(2019)162.